

# A Survey on 3D Gaussian Splatting

Guikun Chen, and Wenguan Wang, *Senior Member, IEEE*

**Abstract**—3D Gaussian splatting (GS) has recently emerged as a transformative technique in the realm of explicit radiance field and computer graphics. This innovative approach, characterized by the utilization of millions of learnable 3D Gaussians, represents a significant departure from mainstream neural radiance field approaches, which predominantly use implicit, coordinate-based models to map spatial coordinates to pixel values. 3D GS, with its explicit scene representation and differentiable rendering algorithm, not only promises real-time rendering capability but also introduces unprecedented levels of editability. This positions 3D GS as a potential game-changer for the next generation of 3D reconstruction and representation. In the present paper, we provide the first systematic overview of the recent developments and critical contributions in the domain of 3D GS. We begin with a detailed exploration of the underlying principles and the driving forces behind the emergence of 3D GS, laying the groundwork for understanding its significance. A focal point of our discussion is the practical applicability of 3D GS. By enabling unprecedented rendering speed, 3D GS opens up a plethora of applications, ranging from virtual reality to interactive media and beyond. This is complemented by a comparative analysis of leading 3D GS models, evaluated across various benchmark tasks to highlight their performance and practical utility. The survey concludes by identifying current challenges and suggesting potential avenues for future research in this domain. Through this survey, we aim to provide a valuable resource for both newcomers and seasoned researchers, fostering further exploration and advancement in applicable and explicit radiance field representation.

**Index Terms**—3D Gaussian Splatting, Explicit Radiance Field, Real-time Rendering, Scene Understanding

## 1 INTRODUCTION

THE objective of image based 3D scene reconstruction is to convert a collection of views or videos capturing a scene into a 3D model that can be processed and understood by computers. This hard and long-standing problem is fundamental for machines to comprehend the complexity of real-world environments, facilitating a wide array of applications such as 3D modeling and animation, robot navigation, historical preservation, augmented/virtual reality, and autonomous driving.

The journey of 3D scene reconstruction began long before the surge of deep learning, with early endeavors focusing on light fields and basic scene reconstruction methods [1]–[3]. These early attempts, however, were limited by their reliance on dense sampling and structured capture, leading to significant challenges in handling complex scenes and lighting conditions. The emergence of structure-from-motion [4] and subsequent advancements in multi-view stereo [5] algorithms provided a more robust framework for 3D scene reconstruction. Despite these advancements, such methods struggled with novel-view synthesis and lacked compatibility with deep scene understanding models. NeRF represents a quantum leap in this progression. By leveraging deep neural networks, NeRF enabled the direct mapping of spatial coordinates to color and density. The success of NeRF hinged on its ability to create continuous, volumetric scene functions, producing results with unprecedented detail and realism. However, as with any burgeoning technology, this implementation came at a cost: i) Computational Intensity. NeRF based methods are computationally intensive [6]–[11], often requiring extensive training times and substantial

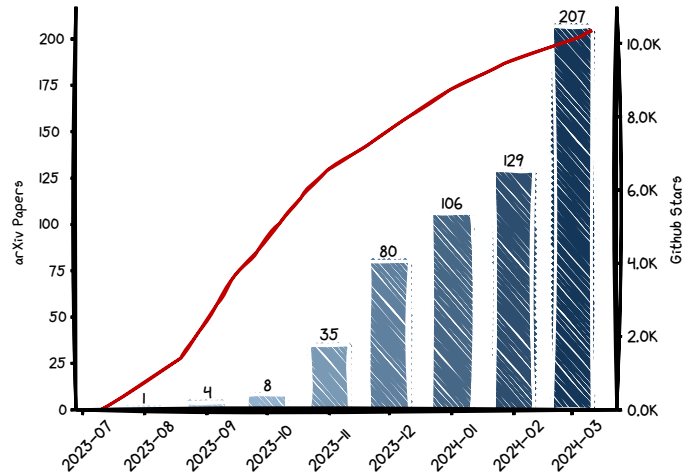


Fig. 1. The number of follow-up arXiv papers and official github stars on 3D GS is increasing every month.

resources for rendering, especially for high-resolution outputs. ii) Editability. Manipulating scenes represented implicitly can be challenging, as direct modifications to the neural network’s weights are not intuitively related to changes in geometric or appearance properties of the scene.

It is in this context that 3D Gaussian splatting (GS) [12] emerges, not merely as an incremental improvement but as a paradigm-shifting approach that redefines the boundaries of scene representation and rendering. While NeRF excelled in creating photorealistic images, the need for faster, more efficient rendering methods was becoming increasingly apparent, especially for applications that are highly sensitive to latency. 3D GS addressed this need by introducing an advanced, explicit scene representation that models a scene using millions of learnable 3D Gaussians

- G. Chen and W. Wang are with College of Computer Science and Technology, Zhejiang University (Email: guikunchen@gmail.com, wenguanwang.ai@gmail.com)
- Corresponding Author: Wenguan Wang

in space. Unlike the implicit, coordinate-based models [13]–[15], 3D GS employs an explicit representation and highly parallelized workflows, facilitating more efficient computation and rendering. The innovation of 3D GS lies in its unique blend of the benefits of differentiable pipelines and point-based rendering techniques [16]–[21]. By representing scenes with learnable 3D Gaussians, it preserves the strong fitting capability of continuous volumetric radiance fields, essential for high-quality image synthesis, while simultaneously avoiding the computational overhead associated with NeRF based methods (*e.g.*, computationally expensive ray-marching, and unnecessary calculations in empty space).

The introduction of 3D GS is not just a technical advancement; it represents a fundamental shift in how we approach scene representation and rendering in computer vision and graphics. By enabling real-time rendering capabilities without compromising on visual quality, 3D GS opens up a plethora of possibilities for applications ranging from virtual reality and augmented reality to real-time cinematic rendering and beyond [22]–[25]. This technology holds the promise of not only enhancing existing applications but also enabling new ones that were previously unfeasible due to computational constraints. Furthermore, 3D GS’s explicit scene representation offers unprecedented flexibility to control the objects and scene dynamics, a crucial factor in complex scenarios involving intricate geometries and varying lighting conditions [26], [27]. This level of editability, combined with the efficiency of the training and rendering process, positions 3D GS as a transformative force in shaping future developments in relevant fields.

In an effort to assist readers in keeping pace with the swift evolution of 3D GS, we provide the first survey on 3D GS, which presents a systematic and timely collection of the most significant recent literature on the topic. Given that 3D GS is a very recent innovation (Fig. 1), our focus is on the diverse developments and contributions that have emerged since its introduction. The selected follow-up works of 3D GS are primarily sourced from top conferences. Our primary goal is to provide a thorough and up-to-date analysis of the theoretical foundations, remarkable developments, and burgeoning applications of 3D GS, highlighting its potential to revolutionize the field. Acknowledging the nascent yet rapidly evolving nature of 3D GS, this survey is inevitably a biased view, but we have strived to pinpoint and discuss the fundamental characteristics of influential works so as to encapsulate primary research trends.

A summary of the structure of this article can be found in Fig. 2, which is presented as follows: Sec. 2 provides a brief background on problem formulation, terminology, and related research domains. Sec. 3 introduces the essential insights of 3D GS, encompassing the novel-view synthesis with 3D Gaussians and the optimization nuances of 3D GS. Sec. 4 presents several fruitful directions that aim to improve the capabilities of the original 3D GS. Sec. 5 unveils the diverse application areas and tasks where 3D GS has made significant impacts, showcasing its versatility. Sec. 6 conducts performance comparison and analysis. Finally, Sec. 7 and 8 highlight the open questions for further research and conclude the survey. We aim to provide a balanced perspective, reflecting the current scope and future potential of 3D GS, and thereby serve as a valuable resource for researchers

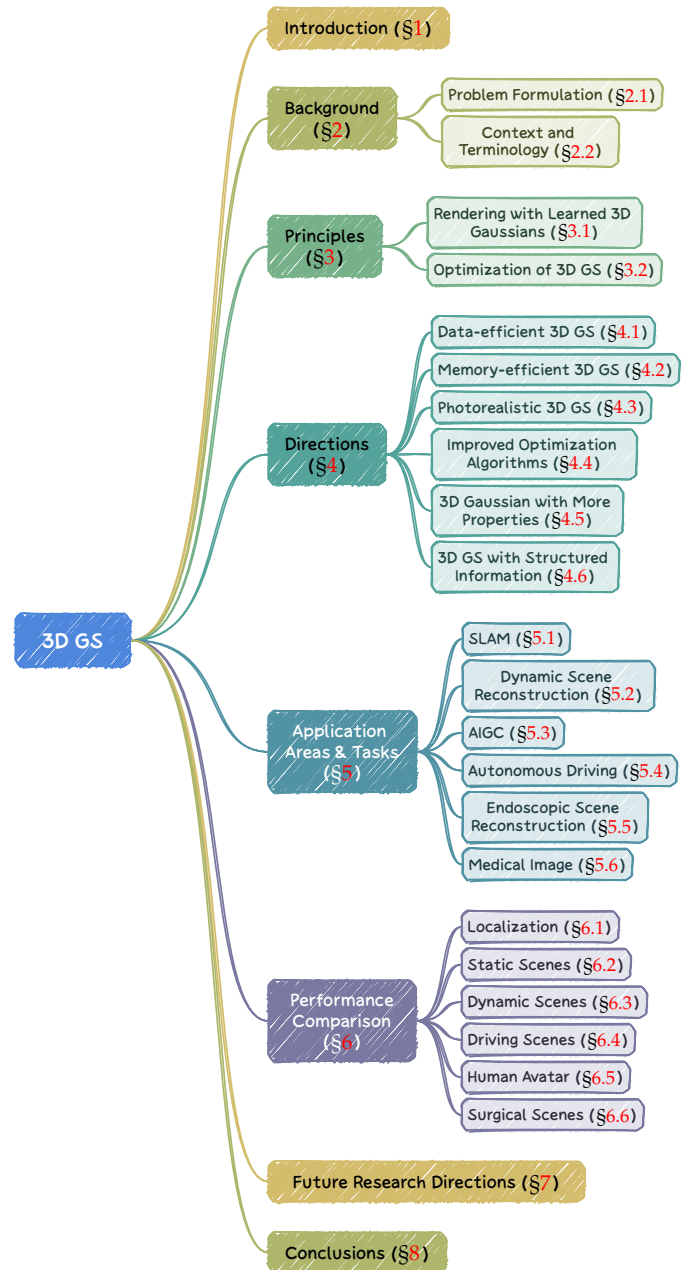


Fig. 2. Structure of the overall review.

and practitioners eager to understand and contribute to this rapidly evolving domain.

## 2 BACKGROUND

In this section, we first provide a brief formulation of radiance fields (Sec. 2.1), a key concept in scene rendering. It outlines two main types of radiance field representations: implicit, like NeRF [15], which uses neural networks for a straightforward yet computationally demanding rendering; and explicit, like grid [28], which employs discrete structures for quicker access but at the cost of higher memory use. Sec. 2.2 further establishes linkages with relevant fields such as scene reconstruction and rendering. For a comprehensive overview of radiance fields, scene reconstruction

and representation, and rendering, please see the excellent surveys [29]–[34].

## 2.1 Problem Formulation

### 2.1.1 Radiance Field

A radiance field is a representation of light distribution in a three-dimensional space, which captures how light interacts with surfaces and materials in the environment [30]. Mathematically, a radiance field can be described as a function  $L : \mathbb{R}^5 \mapsto \mathbb{R}^+$ , where  $L(x, y, z, \theta, \phi)$  maps a point in space  $(x, y, z)$ , and a direction specified by spherical coordinates  $(\theta, \phi)$ , to a non-negative radiance value. Radiance fields can be encapsulated through implicit or explicit representations, each with specific advantages for scene representation and rendering.

### 2.1.2 Implicit Radiance Field

An implicit radiance field represents light distribution in a scene without explicitly defining the geometry of the scene. In the deep learning era, it often uses neural networks to learn a continuous volumetric scene representation [35], [36]. The most prominent example is NeRF [15]. In NeRF, a neural network, typically a multi-layer perceptron (MLP), is used to map a set of spatial coordinates  $(x, y, z)$  and viewing directions  $(\theta, \phi)$  to color and density values. The radiance at any point is not stored explicitly but is computed on-the-fly by querying the MLP. Hence, the function can be written as:

$$L_{\text{implicit}}(x, y, z, \theta, \phi) = \text{MLP}(x, y, z, \theta, \phi). \quad (1)$$

This format allows for a differentiable and compact representation of complex scenes, albeit often at the cost of high computational load during rendering due to volumetric ray marching [12].

### 2.1.3 Explicit Radiance Field

In contrast, an explicit radiance field directly represents the distribution of light in a discrete spatial structure, such as a voxel grid or a set of points [28], [37]. Each element in this structure stores the radiance information for its respective location in space. This approach allows for more direct and often faster access to radiance data but at the cost of higher memory usage and potentially lower resolution. A generic form for an explicit radiance field representation can be written as:

$$L_{\text{explicit}}(x, y, z, \theta, \phi) = \text{DataStructure}[(x, y, z)] \cdot f(\theta, \phi), \quad (2)$$

where `DataStructure` could be in the format of volumes, point clouds, *etc.*  $f(\theta, \phi)$  is a function that modifies the radiance based on the viewing direction.

### 2.1.4 3D Gaussian Splatting: Best-of-Both Worlds

3D GS [12] is an explicit radiance field with the advantages of implicit radiance fields. Concretely, it leverages the strengths of both paradigms by utilizing learnable 3D Gaussians as a flexible and efficient representation. These Gaussians are optimized under the supervision of multi-view images to accurately represent the scene. Such a 3D Gaussian based differentiable pipeline combines the benefits of neural network-based optimization and explicit, structured data storage. This hybrid approach aims to achieve

real-time, high-quality rendering and requires less training time, particularly for complex scenes and high-resolution outputs. The 3D Gaussian representation is formulated as:

$$L_{3\text{DGS}}(x, y, z, \theta, \phi) = \sum_i G(x, y, z, \mu_i, \Sigma_i) \cdot c_i(\theta, \phi), \quad (3)$$

where  $G$  is the Gaussian function with mean  $\mu_i$  and covariance  $\Sigma_i$ , and  $c$  represents the view-dependent color.

## 2.2 Context and Terminology

Several techniques and research disciplines possess a close relationship with 3D GS, which will be described briefly in the following sections.

### 2.2.1 Scene Reconstruction and Rendering

Roughly speaking, scene reconstruction involves creating a 3D model of a scene from a collection of images or other data. Rendering is a more specific term that focuses on transforming computer-readable information (*e.g.*, 3D objects in the scene) to pixel-based images. Early techniques generated realistic images based on the light fields [1]–[3]. The structure-from-motion [4] and multi-view stereo [5] algorithms further advanced this field by estimating 3D structures from image sequences. These historical methods provide a solid foundation for more complex scene reconstruction and rendering techniques [38]–[41].

### 2.2.2 Neural Rendering and Radiance Fields

Neural rendering integrates deep learning with traditional graphics techniques to create photorealistic images [42], [43]. Early attempts utilized convolutional neural networks for estimating blending weights [40] or texture-space solutions [44], [45]. As mentioned in Sec. 2.1.1, the radiance field represents a function that describes the amount of light traveling in every direction through every point in space. NeRFs [10], [11], [15] use neural networks, typically MLPs, to model the radiance fields, enabling detailed and realistic scene rendering.

### 2.2.3 Volumetric Representations and Ray-Marching

Volumetric representations model objects and scenes not just as surfaces but as volumes filled with materials or empty space [46]. This approach allows for a more accurate rendering of phenomena like fog, smoke, or translucent materials. Ray-marching is a technique used with volumetric representations to render images by incrementally tracing the path of light through a volume [13], [14]. NeRF [15] shares the same spirit of volumetric ray-marching and introduces importance sampling and positional encoding to improve the quality of synthesized images. While providing high-quality results, volumetric ray-marching is computationally expensive, motivating the search for more efficient methods like 3D GS.

### 2.2.4 Point-based Rendering

Point-based rendering is a technique for visualizing 3D scenes using points rather than traditional polygons. This method is particularly effective for rendering complex, unstructured, or sparse geometric data. Points can be augmented with additional properties like learnable neural

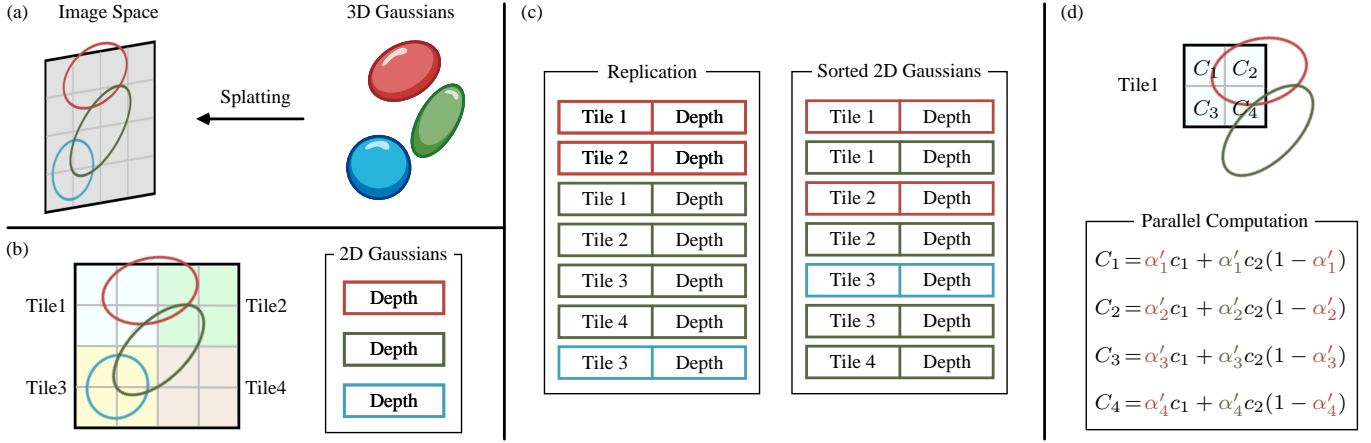


Fig. 3. An illustration of the forward process of 3D GS (Sec. 3.1). (a) The splatting step projects 3D Gaussians into image space. (b) 3D GS divides the image into multiple non-overlapping patches, *i.e.*, tiles. (c) 3D GS replicates the Gaussians which cover several tiles, assigning each copy an identifier, *i.e.*, a tile ID. (d) By rendering the sorted Gaussians, we can obtain all pixels within the tile. Note that the computational workflows for pixels and tiles are independent and can be done in parallel. Best viewed in color.

descriptors [47], [48], and rendered efficiently [49], [50], but this approach suffers from issues like holes in the rendering or aliasing effects. 3D GS [12] extends this concept by using anisotropic Gaussians for a more continuous and cohesive representation of the scene. More details will be further discussed in Sec. 3.

### 3 3D GAUSSIAN SPLATTING: PRINCIPLES

3D GS offers a breakthrough in real-time, high-resolution image rendering, without relying on neural components. This section aims to provide essential insights of 3D GS. We first elaborate on how 3D GS synthesizes an image given well-constructed 3D Gaussians in Sec. 3.1, *i.e.*, the forward process of 3D GS. Then, we introduce how to obtain well-constructed 3D Gaussians for a given scene in Sec. 3.2, *i.e.*, the optimization process of 3D GS.

#### 3.1 Novel-view Synthesis with Learned 3D Gaussians

Consider a scene represented by (millions of) optimized 3D Gaussians. The objective is to generate an image from a specified camera pose. Recall that NeRFs approach this task through computationally demanding volumetric ray-marching, sampling 3D space points per pixel. Such a paradigm struggles with high-resolution image synthesis, failing to achieve real-time rendering, especially for platforms with limited computing resources [12]. By contrast, 3D GS begins by projecting these 3D Gaussians onto a pixel-based image plane, a process termed “splatting” (see Fig. 3a). Afterwards, 3D GS sorts these Gaussians and computes the value for each pixel. As shown in Fig. 4, the rendering of NeRFs and 3D GS can be viewed as an inverse process of each other. In what follows, we begin with the definition of a 3D Gaussian, which is the minimal element of the scene representation in 3D GS. Next, we describe how these 3D Gaussians can be used for differentiable rendering. Finally, we introduce the acceleration technique used in 3D GS, which is the key to fast rendering.

• **Properties of 3D Gaussian.** A 3D Gaussian is characterized by its center (position)  $\mu$ , opacity  $\alpha$ , 3D covariance

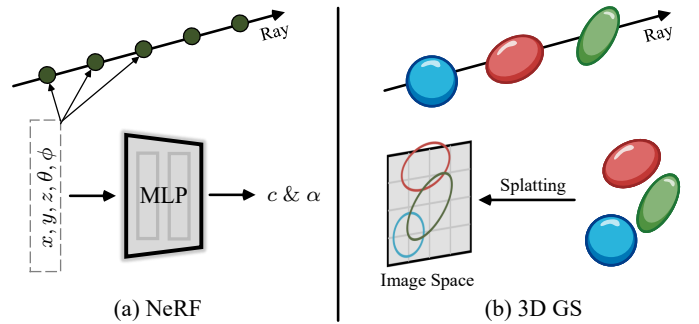


Fig. 4. NeRFs vs. 3D GS. (a) NeRF samples along the ray and then queries the MLP to obtain corresponding colors and opacities, which can be seen as a *backward* mapping (ray tracing). (b) In contrast, 3D GS projects all 3D Gaussians into the image space (*i.e.*, splatting) and then performs parallel rendering, which can be viewed as a *forward* mapping (splatting and rasterization). Best viewed in color.

matrix  $\Sigma$ , and color  $c$ .  $c$  is represented by spherical harmonics for view-dependent appearance. All the properties are learnable and optimized through back-propagation.

• **Frustum Culling.** Given a specified camera pose, this step determines which 3D Gaussians are outside the camera’s frustum. By doing so, 3D Gaussians outside the given view will not be involved in the subsequent computation, thus saving computational resources.

• **Splatting.** In this step, 3D Gaussians (ellipsoids) are projected into the 2D image space (ellipses) for rendering. Given the viewing transformation  $\mathbf{W}$  and 3D covariance matrix  $\Sigma$ , the projected 2D covariance matrix  $\Sigma'$  is computed using:

$$\Sigma' = \mathbf{J}\mathbf{W}\Sigma\mathbf{W}^\top\mathbf{J}^\top, \quad (4)$$

where  $\mathbf{J}$  is the Jacobian of the affine approximation of the projective transformation [12], [51].

• **Rendering by Pixels.** Before delving into the final version of 3D GS which utilizes several techniques to boost parallel computation, we first elaborate on its simpler form to offer insights into its basic working mechanism. Given the position of a pixel  $x$ , its distance to all overlapping Gaus-

sians, *i.e.*, the depths of these Gaussians, can be computed through the viewing transformation  $\mathbf{W}$ , forming a sorted list of Gaussians  $\mathcal{N}$ . Then, alpha compositing is adopted to compute the final color of this pixel:

$$C = \sum_{i \in \mathcal{N}} c_i \alpha'_i \prod_{j=1}^{i-1} (1 - \alpha'_j), \quad (5)$$

where  $c_i$  is the learned color. The final opacity  $\alpha'_i$  is the multiplication result of the learned opacity  $\alpha_i$  and the Gaussian, defined as follows:

$$\alpha'_i = \alpha_i \times \exp\left(-\frac{1}{2}(\mathbf{x}' - \boldsymbol{\mu}'_i)^\top \boldsymbol{\Sigma}'_i{}^{-1}(\mathbf{x}' - \boldsymbol{\mu}'_i)\right), \quad (6)$$

where  $\mathbf{x}'$  and  $\boldsymbol{\mu}'_i$  are coordinates in the projected space. It is a reasonable concern that the rendering process described could be slower compared to NeRFs, given that generating the required sorted list is hard to parallelize. Indeed, this concern is justified; rendering speeds can be significantly impacted when utilizing such a simplistic, pixel-by-pixel approach. To achieve real-time rendering, 3D GS makes several concessions to accommodate parallel computation.

- **Tiles (Patches).** To avoid the cost computation of deriving Gaussians for each pixel, 3D GS shifts the precision from pixel-level to patch-level detail. Concretely, 3D GS initially divides the image into multiple non-overlapping patches, called “tiles” in the original paper [12]. Fig. 3b provides an illustration of tiles. Each tile comprises  $16 \times 16$  pixels as suggested in [12]. 3D GS further determines which **tiles** intersect with these projected Gaussians. Given that a projected Gaussian may cover several tiles, a logical method involves replicating the Gaussian, assigning each copy an identifier (*i.e.*, a tile ID) for the relevant tile.

- **Parallel Rendering.** After replication, 3D GS combines the respective tile ID with the depth value obtained from the view transformation for each Gaussian. This results in an unsorted list of bytes where the upper bits represent the tile ID and the lower bits signify depth. By doing so, the sorted list can be directly utilized for rendering (*i.e.*, alpha compositing). Fig. 3c and Fig. 3d provide the visual demonstration of such concepts. It’s worth highlighting that rendering each tile and pixel occurs **independently**, making this process highly suitable for parallel computations. An additional benefit is that each tile’s pixels can access a common **shared memory** and maintain a **uniform read sequence**, enabling parallel execution of alpha compositing with increased efficiency. In the official implementation of the original paper [12], the framework regards the processing of tiles and pixels as analogous to the blocks and threads, respectively, in CUDA programming architecture.

In a nutshell, 3D GS introduces several approximations during the forward processing phase to enhance computational efficiency while maintaining a high standard of image synthesis quality.

## 3.2 Optimization of 3D Gaussian Splatting

At the heart of 3D GS lies an optimization procedure devised to construct a copious collection of 3D Gaussians that accurately captures the scene’s essence, thereby facilitating free-viewpoint rendering. On the one hand, the properties of 3D Gaussians should be optimized via differentiable

rendering to fit the textures of a given scene. On the other hand, the number of 3D Gaussians that can represent a given scene well is unknown in advance. One promising avenue is to let the neural network automatically learn the density of 3D Gaussians. We will introduce how to optimize the properties of each Gaussian in Sec. 3.2.1 and how to control the density of the Gaussians in Sec. 3.2.2. The two procedures are interleaved within the optimization workflow. Since there are many manually set hyperparameters in the optimization process, we omit the notations of most hyperparameters for clarity.

### 3.2.1 Parameter Optimization

- **Loss Function.** Once the synthesis of the image is completed, the difference between the rendered image and ground truth can be measured. All learnable parameters are optimized by stochastic gradient descent using the L1 and D-SSIM loss functions:

$$\mathcal{L} = (1 - \lambda)\mathcal{L}_1 + \lambda\mathcal{L}_{\text{D-SSIM}}, \quad (7)$$

where  $\lambda$  is a weighting factor. The loss function of 3D GS is slightly different from that of NeRFs. NeRFs typically calculate losses at the pixel level rather than the image level because of the costly ray-marching.

- **Parameter Update.** Most properties of a 3D Gaussian can be optimized directly through back-propagation. It is essential to note that directly optimizing the covariance matrix  $\boldsymbol{\Sigma}$  can result in a non-positive semi-definite matrix, which would not adhere to the physical interpretation typically associated with covariance matrices. To circumvent this issue, 3D GS chooses to optimize a quaternion  $\mathbf{q}$  and a 3D vector  $\mathbf{s}$ .  $\mathbf{q}$  and  $\mathbf{s}$  represent rotation and scale, respectively. This approach allows the covariance matrix  $\boldsymbol{\Sigma}$  to be reconstructed as follows:

$$\boldsymbol{\Sigma} = \mathbf{R}\mathbf{S}\mathbf{S}^\top\mathbf{R}^\top, \quad (8)$$

where  $\mathbf{R}$  and  $\mathbf{S}$  denote the rotation and scaling matrix derived from  $\mathbf{q}$  and  $\mathbf{s}$ , respectively. There is a complex computational graph to obtain the opacity  $\alpha$ , *i.e.*,  $\mathbf{q}$  and  $\mathbf{s} \mapsto \boldsymbol{\Sigma}$ ,  $\boldsymbol{\Sigma} \mapsto \boldsymbol{\Sigma}'$ , and  $\boldsymbol{\Sigma}' \mapsto \alpha$ . To avoid the cost of automatic differentiation, 3D GS derives the gradients for  $\mathbf{q}$  and  $\mathbf{s}$  so as to compute them directly during optimization.

### 3.2.2 Density Control

- **Initialization.** 3D GS starts with the initial set of sparse points from SfM or random initialization. Afterwards, point densification and pruning are adopted to control the density of 3D Gaussians.

- **Point Densification.** In the point densification phase, 3D GS adaptively increases the density of Gaussians to better capture the details of a scene. This process particularly focuses on areas with missing geometric features or regions where Gaussians are too spread out. The densification procedure will be performed at regular intervals (*i.e.*, after a certain number of training iterations), focusing on those Gaussians with large view-space positional gradients (*i.e.*, above a specific threshold). It involves either cloning small Gaussians in under-reconstructed areas or splitting large Gaussians in over-reconstructed regions. For cloning, a copy of the Gaussian is created and moved towards the positional

gradient. For splitting, a large Gaussian is replaced with two smaller ones, reducing their scale by a specific factor. This step seeks an optimal distribution and representation of Gaussians in the 3D space, enhancing the overall quality of the reconstruction.

- **Point Pruning.** The point pruning stage involves the removal of superfluous or less impactful Gaussians, which can be viewed as a regularization process to some extent. This step is executed by eliminating Gaussians that are virtually transparent (with  $\alpha$  below a specified threshold) and those that are excessively large in either world-space or view-space. In addition, to prevent unjustified increases in Gaussian density near input cameras, the alpha value of the Gaussians is set close to zero after a certain number of iterations. This allows for a controlled increase in the density of necessary Gaussians while enabling the culling of redundant ones. The process not only helps in conserving computational resources but also ensures that the Gaussians in the model remain precise and effective for the representation of the scene.

## 4 3D GAUSSIAN SPLATTING: DIRECTIONS

The last months have witnessed significant advancements in the realm of 3D GS. It brings us great pleasure to witness the fruition of the research directions we noted in our previous editions. In the subsequent sections, we seek to elaborate on select extended versions of 3D GS. These are: i) Data-efficient 3D GS [52]–[61] (Sec. 4.1), ii) Memory-efficient 3D GS [62]–[68] (Sec. 4.2), iii) Photorealistic 3D GS [69]–[85] (Sec. 4.3), iv) Improved Optimization Algorithms [82], [86]–[90] (Sec. 4.4), v) 3D Gaussian with More Properties [91]–[97] (Sec. 4.5), and vi) 3D GS with Structured Information [98]–[100] (Sec. 4.6).

### 4.1 Data-efficient 3D GS

A notable issue of 3D GS is the emergence of artifacts in areas with insufficient observational data. This challenge is a prevalent limitation in radiance field rendering, where sparse data often leads to inaccuracies in reconstruction. From a practical perspective, reconstructing scenes from limited viewpoints is of significant interest, particularly for their potential to enhance realism and user experience with minimal input.

Two primary strategies are used for data-efficient 3D GS. i) The first introduces additional constraints such as depth information to enhance the detail and global consistency. For example, DNGaussian [56] introduced a depth-regularized approach to address the challenge of geometry degradation in sparse input views through hard and soft depth regularization and global-local depth normalization. It rectified the geometry using depth information extracted from pre-trained monocular depth estimators and optimized the positioning of Gaussian primitives without changing their shape, ensuring a balance between detailed color appearance and coherent scene geometry. ii) The second generates 3D Gaussians that can be used for rendering directly without optimization, by using deep neural networks. This paradigm typically requires multiple views for training but can reconstruct the 3D scene with only one input image. For

instance, PixelSplat [54] proposed to sample Gaussians from dense probability distributions. It incorporated a multi-view epipolar transformer and a reparameterization trick to avoid local minima and maintain gradient flow. Splatter Image [55] applied GS in a monocular setting through a learning-based approach, utilizing a 2D image-to-image network that maps an input image to a 3D Gaussian per pixel. Gamba [61] introduced an end-to-end, Mamba based sequential network [101] to generate 3D Gaussians with linear scalability. Note that this paradigm is mainly focused on the reconstruction of objects, and its generalizability leaves a lot of room for improvement.

### 4.2 Memory-efficient 3D GS

While 3D GS demonstrates remarkable capabilities, its scalability poses significant challenges, particularly when juxtaposed with NeRF-based methods. The latter benefits from the simplicity of storing merely the parameters of a learned MLP. This scalability issue becomes increasingly acute in the context of large-scale scene management, where the computational and memory demands escalate substantially. Consequently, there is an urgent need to optimize memory utilization during both the training phase and the storage of the model.

There are two main directions to reduce memory usage. i) The first involves reducing the number of 3D Gaussians, *i.e.*, pruning insignificant 3D Gaussians. For example, LightGaussian [62] pruned insignificant Gaussians based on their contribution to scene reconstruction. Lee *et al.* [64] introduced a new volume-based masking strategy that efficiently reduces the quantity of Gaussians required for scene representation without compromising performance. ii) The second category focuses on compressing the memory usage of 3D Gaussian properties. For instance, LightGaussian [62] introduced vector quantization [102] for attribute quantization to achieve lower bitwidth representations. Lee *et al.* [64] employed a grid-based neural field for a more compact representation of view-dependent colors and utilizes a codebook approach for the concise encoding of Gaussian geometries. Niedermayr *et al.* [67] compressed color and Gaussian parameters into compact codebooks, using sensitivity measures for effective quantization and fine-tuning, coupled with entropy encoding to utilize spatial coherence.

### 4.3 Photorealistic 3D GS

The current rendering pipeline of 3D GS (Sec. 3.1) is straightforward and involves several drawbacks. For instance, the simple visibility algorithm may lead to a drastic switch in the depth/blending order of Gaussians. The realness of rendered images (*e.g.*, aliasing, reflections, and artifacts) can be further optimized.

Here we list several key points for enhancing realness. i) Varying Resolutions. Due to the discrete sampling paradigm (viewing each pixel as a single point instead of an area), 3D GS is susceptible to aliasing when dealing with varying resolutions, which leads to blurring or jagged edges. Yan *et al.* [71] argued that this is mainly because traditional rendering methods cannot effectively manage the disparity between the sampling frequency of pixels and the high-frequency details of the scene, leading to visual artifacts

and performance issues. Hence, they introduced multi-scale 3D GS, where the scene is represented using Gaussians of varying sizes. Analytic-Splatting [83] adopted an analytic approximation of the Gaussian integral within the pixel area, leveraging a conditioned logistic function for the cumulative distribution function to better capture the intensity response of pixels. It aimed to make the rendering process sensitive to changes in pixel footprints at different resolutions, thereby enhancing anti-aliasing capabilities and preserving high-quality details. ii) Reflections. Achieving realistic rendering of reflective materials is a hard and long-standing problem in 3D scene reconstruction. GaussianShader [72] enhanced neural rendering for scenes with reflective surfaces by integrating a simplified shading function with 3D Gaussians. iii) Geometry. One limitation of 3D GS is the neglect of underlying scene geometry and structure, particularly in complex scenes and under varying view and lighting conditions. Scaffold-GS [73] introduced a sparse grid of anchor points to organize local 3D Gaussians, which are dynamically adjusted for attributes like opacity and color based on the viewer’s perspective and distance. This method enhanced scene representation through a hierarchical structure informed by scene geometry.

#### 4.4 Improved Optimization Algorithms

The anisotropic Gaussians, while beneficial for representing complex geometries, can create undesirable visual artifacts. For example, those large 3D Gaussians, especially in regions with view-dependent appearance, can cause popping artifacts, where visual elements abruptly appear or disappear, breaking the immersion. Further, incorporating additional regularization (*e.g.*, geometry [82], [88] and frequency [89]) and improving the optimization process of 3D GS (Sec. 3.2) may accelerate convergence, smooth visual noise, and improve quality of rendered images.

Three main directions stand out for improving the optimization of 3D GS. i) Introducing Additional Regularization. 3D GS often faces challenges with over-reconstruction, where sparse, large 3D Gaussians cause blur and artifacts due to poor representation in high-variance regions. To address this, FreGS [89] introduced a progressive frequency regularization method, which refines Gaussian densification from a frequency perspective. In terms of the global geometry consistency, GeoGaussian [82] focused on preserving the geometry of non-textured regions like walls and furniture, which tend to degrade over time. ii) Improving Optimization Algorithm. In addressing the challenges of scale and structural inhomogeneity in 3D GS, which result in blurred boundaries and sparse point clouds in untextured areas, Feng *et al.* [90] introduced an advanced splitting algorithm. This algorithm decomposed an  $N$ -dimensional Gaussian into two, aiming to preserve essential mathematical characteristics (*e.g.*, opacity, position, and covariance) and enhancing surface conformity and uniformity. iii) Relaxing Constraints in Optimization. Reliance on external tools/algorithms for can introduce errors and cap the system’s performance potential. For instance, structure-from-motion (SfM), commonly used in the initialization process, are error-prone and struggle with complex scenes. Yang *et al.* [86] proposed COLMAP-Free 3D GS, which introduces video

stream continuity and an explicit point cloud representation so as to eliminate the need for SfM preprocessing.

#### 4.5 3D Gaussian with More Properties

Despite impressive, the properties of 3D Gaussian (Sec. 3.1) are designed to be used for novel-view synthesis only. By augmenting 3D Gaussian with additional properties, such as linguistic [91]–[93], semantic/instance [94]–[96], and spatial-temporal [97] properties, 3D GS demonstrates its considerable potential to revolutionize various domains.

Here we list several interesting applications using 3D Gaussians with specially designed properties. i) Language Embedded Scene Representation. Due to the high computational and memory demands of current language-embedded scene representations, Shi *et al.* [91] proposed a quantization scheme that augments 3D Gaussian with streamlined language embeddings instead of the original high-dimensional embeddings. This method also mitigated semantic ambiguity and enhanced the precision of open-vocabulary querying by smoothing out semantic features across different views, guided by uncertainty values. ii) Scene Understanding and Editing. Feature 3DGS [94] integrated 3D GS with feature field distillation from 2D foundation models. By learning a lower-dimensional feature field and applying a lightweight convolutional decoder for upsampling, Feature 3DGS achieved faster training and rendering speeds while enabling high-quality feature field distillation, supporting applications like semantic segmentation and language-guided editing. iii) Spatiotemporal Modeling. To capture the complex spatial and temporal dynamics of 3D scenes, Yang *et al.* [97] conceptualized spacetime as a unified entity and approximates the spatiotemporal volume of dynamic scenes using a collection of 4D Gaussians. The proposed 4D Gaussian representation and corresponding rendering pipeline are capable of modeling arbitrary rotations in space and time and allow for end-to-end training.

#### 4.6 3D GS with Structured Information

In addition to augmenting 3D Gaussian with additional properties, another promising avenue of adapting to downstream tasks is to introduce structured information (*e.g.*, spatial MLPs and grids) tailored for specific applications.

Next we showcase various fascinating uses of 3D GS with specially devised structured information. i) Facial Expression Modeling. Considering the challenge of creating high-fidelity 3D head avatars under sparse view conditions, Gaussian Head Avatar [100] introduced controllable 3D Gaussians and an MLP-based deformation field. Concretely, it captured detailed facial expressions and dynamics by optimizing neutral 3D Gaussians alongside the deformation field, thus ensuring both detail fidelity and expression accuracy. ii) Spatiotemporal Modeling. Yang *et al.* [98] proposed to reconstruct dynamic scenes with deformable 3D Gaussians. The deformable 3D Gaussians are learned in a canonical space, coupled with a deformation field (*i.e.*, a spatial MLP) that models the spatial-temporal dynamics. The proposed method also incorporated an annealing smoothing training mechanism to enhance temporal smoothness without additional computational costs. iii) Style Transfer.

Saroha *et al.* [103] proposed GS in style, an advanced approach for real-time neural scene stylization. To maintain a cohesive stylized appearance across multiple views without compromising on rendering speed, they used pre-trained 3D Gaussians coupled with a multi-resolution hash grid and a small MLP to produce stylized views. Such a fast, view-consistent pipeline makes it particularly suited for AR/VR applications.

## 5 APPLICATION AREAS AND TASKS

The transformative potential of 3D GS extends far beyond its theoretical and computational advancements. This section delves into the diverse and groundbreaking application areas where 3D GS is making a significant impact, such as robotics (Sec. 5.1), dynamic scene reconstruction and representation (Sec. 5.2), AI-generated content (Sec. 5.3), autonomous driving (Sec. 5.4), medical systems (Sec. 5.5 and Sec. 5.6), and even other scientific disciplines. The applications of 3D GS demonstrate its versatility to revolutionize various fields. Here, we outline some of the most notable application domains, providing insights into how 3D GS is shaping new frontiers in each area.

### 5.1 Simultaneous Localization and Mapping (SLAM)

SLAM is a computational problem central to robotics and autonomous systems. It involves the challenge of a robot or a device understanding its position in an unknown environment while simultaneously mapping the environment's layout [104]. SLAM is critical in various applications, including autonomous vehicles, augmented reality, and robotic navigation [105], [106]. The core of SLAM is to create a map of an unknown environment and determine the device's location on this map in real-time. As a result, SLAM poses great challenges for computationally intensive scene representation techniques, yet serves as a good testbed for 3D GS.

3D GS enters the SLAM domain as an innovative approach for scene representation. Traditional SLAM systems often use point/surfel clouds or voxel grids to represent environments [107]–[114]. In contrast, 3D GS utilizes anisotropic Gaussians to better represent environments. Recent innovative studies have employed 3D Gaussian Splatting in SLAM [115]–[121], showcasing the potential and versatility of this paradigm. An intuitive way is to use 3D Gaussian directly as the basic representation of the dense map and optimize the tracking process. For instance, GS-SLAM [118] adopted an adaptive strategy to add or remove 3D Gaussians so as to optimize scene geometry reconstruction and improve the mapping of previously observed areas. It also implemented a coarse-to-fine scheme for efficient camera pose tracking by selecting reliable 3D Gaussians. SplaTAM [119] integrated a straightforward online tracking and mapping method that leverages a silhouette mask for capturing the presence of scene density, facilitating fast rendering, dense optimization, and structured map expansion. GSSLAM [116] optimized 3D Gaussians directly for robust camera tracking and introduced geometric verification and regularization to tackle reconstruction ambiguities. On the other hand, designing advanced scene representations is

worth exploring. For example, Photo-SLAM [115] proposed a hyper primitives map, which combines explicit geometric features for precise localization with implicit photometric features for texture mapping.

### 5.2 Dynamic Scene Reconstruction

Dynamic scene reconstruction refers to the process of capturing and representing the three-dimensional structure and appearance of a scene that changes over time [122]–[125]. This involves creating a digital model that accurately reflects the geometry, motion, and visual aspects of the objects in the scene as they evolve. Dynamic scene reconstruction is crucial in various applications, *e.g.*, virtual and augmented reality, 3D animation, and computer vision.

To extend the concept of 3D GS to dynamic scenes, a straightforward approach is to incorporate the temporal dimension, allowing for the representation and rendering of scenes that change over time. 3D GS based methods [97]–[99], [126]–[136] for dynamic scene reconstruction can generally be divided into two main categories. The first category utilizes additional structural information like spatial MLPs or grids (Sec. 4.6). For example, Yang *et al.* [98] first proposed deformable 3D Gaussians tailored for dynamic scenes. These 3D Gaussians are learned in a canonical space and can be used to model spatial-temporal deformation with an implicit deformation field (implemented as an MLP). SC-GS [131] leveraged sparse control points and a deformation MLP to capture and represent the dynamics of 3D scenes. By decomposing motion into compact, learnable transformations applied to these control points, SC-GS achieved efficient and coherent motion modeling and allowed for motion editing. On the other hand, the second category is based on the idea that scene changes can be encoded into the 3D Gaussian representation with a specially designed rendering process (Sec. 4.5). For instance, Luiten *et al.* [130] introduced dynamic 3D Gaussians to model dynamic scenes by keeping the characteristics of 3D Gaussians (*i.e.*, color, opacity, and size) constant over time while allowing their positions and orientations to change. Yang *et al.* [97] designed a 4D Gaussian representation, where additional properties are used to represent 4D rotations and spherical harmonics, to approximate the spatial-temporal volume of scenes.

### 5.3 AI-Generated Content (AIGC)

AIGC refers to the digital content that is autonomously created or significantly altered by artificial intelligence systems, particularly in the fields of computer vision, natural language processing, and machine learning. AIGC is characterized by its ability to simulate, extend, or augment human-generated content, enabling applications that range from realistic image synthesis to dynamic narrative creation. The significance of AIGC lies in its transformative potential across various sectors, including entertainment, education, and technology development [137]–[140]. It's a pivotal element in the evolving landscape of digital content creation, offering scalable, customizable, and often more efficient alternatives to traditional methods.

This explicit nature of 3D GS facilitates real-time rendering capabilities and unprecedented levels of control and



editability, making it highly relevant for and AIGC applications. The explicit scene representations and differentiable rendering algorithms of 3D GS align perfectly with the requirements of AIGC for generating high-fidelity, real-time, and editable content, crucial for applications in virtual reality, interactive media, and beyond. Recent works have effectively utilized 3D GS in conjunction with fields like generative models [141]–[159], avatars [160]–[185], and scene editing [94]–[96], [131]–[133], [186]–[192]. For instance, DreamGaussian [142] accelerated the generation of photorealistic 3D assets from single-view image through a three-step process: a diffusion based generative GS process, followed by an efficient algorithm for mesh extraction from 3D Gaussians based on local density querying, and finally a UV-space refinement stage to improve texture details. By combining 3D GS with a parametric morphable face model, GaussianAvatars [169] offered enhanced fidelity and flexibility in avatar animation, significantly improving upon current methods in novel-view rendering and expression reenactment. GaussianEditor [186] introduced Gaussian semantic tracing for precise editing, hierarchical GS for stabilized results under random generative guidance, and a targeted editing strategy for efficient object removal and integration.

## 5.4 Autonomous Driving

Autonomous driving aims to allow vehicles to navigate and operate without human intervention. These vehicles are equipped with a suite of sensors, including cameras, light detection and ranging (LiDAR), and radar, combined with advanced algorithms, machine learning models, and significant computational power [201]–[204]. The central aim is to perceive the environment, make informed decisions, and execute maneuvers safely and efficiently [205]–[208].

Autonomous vehicles need to perceive and interpret their surroundings to navigate safely. This involves reconstructing the driving scene in real-time, accurately identifying static and dynamic objects, and understanding their spatial relationships and movements [209]–[211]. In dynamic driving scenes, the environment is continuously changing due to moving objects like other vehicles, pedestrians, or animals [212]. Accurately reconstructing these scenes in real-time is crucial for safe navigation but is challenging due to the complexity and variability of the elements involved. In autonomous driving, 3D GS can be utilized to reconstruct a scene by blending data points (such as those obtained from sensors like LiDAR) into a cohesive and continuous representation. This is particularly useful for handling the varying densities of data points and ensuring a smooth and accurate reconstruction of both the static background and dynamic objects in a scene. To reconstruct complex 3D scenes from sparse sensor data, especially at high speeds and with moving objects, mainstream frameworks separated the urban/street scene into static and dynamic elements, where the dynamic elements are modeled using a composite dynamic Gaussian graph [213], point clouds combined with semantic logits [214], or physically constrained models [215].

## 5.5 Endoscopic Scene Reconstruction

Surgical 3D reconstruction represents a fundamental task in the landscape of robot-assisted minimally invasive surgery, aimed at enhancing intraoperative navigation, preoperative planning, and educational simulations through precise modeling of dynamic surgical scenes. Pioneering the integration of cutting-edge dynamic radiance fields into this domain, recent advancements have focused on surmounting the inherent challenges of single-viewpoint video reconstructions – such as occlusions by surgical instruments and sparse viewpoint diversity within the confined spaces of endoscopic exploration [216]–[218]. Despite the progress, the call for high fidelity in tissue deformability and topological variance remains, coupled with the pressing demand for faster rendering to bridge the utility in real-time applications [219]–[221]. This synthesis of immediacy and precision in reconstructing deformable tissues from endoscopic videos is essential in propelling robotic surgery towards reduced patient trauma and augmented reality applications, ultimately fostering a more intuitive surgical environment and nurturing the future of surgical automation and robotic proficiency.

Compared to typical dynamic scene reconstruction, endoscopic scene reconstruction faces unique challenges, *e.g.*, sparse training data due to constrained camera movement in confined space, unobserved regions due to tool occlusion, and pronounced non-rigid deformation of tissues. Existing approaches mainly used additional depth guidance to infer the geometry of tissues. For instance, Endo-4DGS [219] introduced a temporal component to 3D GS, utilizing a lightweight MLP to model temporal deformations, thereby facilitating the reconstruction of dynamic surgical scenes. By generating pseudo-depth maps from monocular views via an off-the-shelf depth estimator, it overcame the limitations of stereo camera setups and improved the depth-guided reconstruction process. Similarly, EndoGaussian [220] introduced two new strategies: holistic Gaussian initialization, which uses depth estimation models to predict depth maps from binocular/monocular image sequences, facilitating dense Gaussian initialization through pixel re-projection and combination; and spatiotemporal Gaussian tracking, which models scene dynamics using a deformation field, consisting of an efficient encoding voxel and a lightweight deformation decoder, and thus enables effective Gaussian tracking with reduced training and rendering efforts. EndoGS [221] also integrated depth-guided supervision with spatial-temporal weight masks and surface-aligned regularization terms to enhance the quality and speed of 3D tissue rendering while addressing tool occlusion. By utilizing a streamlined Gaussian representation combined with differentiable rasterization, EndoGSLAM [222] provided precise camera tracking, detailed 3D tissue reconstruction, and real-time visualization to support surgeons during minimally invasive procedures.

## 5.6 Medical Image

In the realm of medical imaging, X-ray stands as a foundational technique that employs electromagnetic radiation to capture images of the body’s internal structure [223]. This method hinges on the differential absorption of X-rays

TABLE 1

**Quantitative localization results** (§6.1) on Replica [193], in terms of absolute trajectory error (ATE, cm). \* denotes numbers taken from [117]. (The three best scores are marked in **red**, **blue**, and **green**, respectively. These notes also apply to the other tables.)

Method	GS	Room0	Room1	Room2	Office0	Office1	Office2	Office3	Office4	Average
F2F* [194] [ICCV17]		1.64	1.92	2.80	2.48	0.80	4.55	2.64	2.27	2.38
iMAP [195] [ICCV21]		3.12	2.54	2.31	1.69	1.03	3.99	4.05	1.93	2.58
Vox-Fusion [196] [ISMAR22]		1.37	4.70	1.47	8.48	2.04	2.58	1.11	2.94	3.09
NICE-SLAM [197] [CVPR22]		0.97	1.31	1.07	0.88	1.00	1.06	1.10	1.13	1.06
ESLAM [198] [CVPR23]		0.71	0.70	0.52	0.57	0.55	0.58	0.72	<b>0.63</b>	0.63
Point-SLAM [199] [ICCV23]		0.61	<b>0.41</b>	0.37	<b>0.38</b>	<b>0.48</b>	<b>0.54</b>	0.69	0.72	<b>0.52</b>
Co-SLAM [200] [CVPR23]		0.70	0.95	1.35	0.59	0.55	2.03	1.56	0.72	1.00
Gaussian-SLAM [117] [arXiv]	✓	3.35	8.74	3.13	1.11	0.81	0.78	1.08	7.21	3.27
GSSLAM [116] [CVPR24]	✓	<b>0.47</b>	<b>0.43</b>	<b>0.31</b>	0.70	0.57	<b>0.31</b>	<b>0.31</b>	3.20	0.79
SplaTAM [119] [CVPR24]	✓	<b>0.31</b>	<b>0.40</b>	<b>0.29</b>	<b>0.47</b>	<b>0.27</b>	<b>0.29</b>	<b>0.32</b>	<b>0.55</b>	<b>0.36</b>
GS-SLAM [118] [CVPR24]	✓	<b>0.48</b>	0.53	<b>0.33</b>	<b>0.52</b>	<b>0.41</b>	0.59	<b>0.46</b>	<b>0.70</b>	<b>0.50</b>

by various tissues, rendering visible the contrasts between bones, organs, and other internal elements without necessitating surgical intervention. Computed tomography (CT), an advanced iteration of X-ray imaging, enhances this process through the acquisition of multiple X-ray images from diverse angles around the patient. These images are then used to model a 3D representation (*e.g.*, volumes), offering detailed cross-sectional views akin to slicing through the body layer by layer [224], [225]. This capability significantly amplifies the precision of diagnostics, allowing for the effective identification, monitoring, and management of medical conditions.

3D GS can be used directly for X-ray novel view synthesis, with a minor modification of the Gaussian’s attributes, *i.e.*, from spherical harmonics to other functions to represent the absorption of X-ray radiation. Current works can be categorized according to their formulation of the scanned objects: i) *w/o* Volumes. X-Gaussian [226] proposed two main innovations: a redesigned radiative Gaussian point cloud model that captures the isotropic nature of X-ray radiation, utilizing a radiation intensity response function in place of spherical harmonics to model radiation intensity independently of view direction; and an angle-pose cuboid uniform initialization strategy for efficient point cloud initialization, leveraging X-ray scanner parameters to reduce training time significantly. ii) *with* Volumes. To reduce the radiation dose of traditional CT scans, Li *et al.* [227] used the capability of 3D Gaussians for sparse-view CT reconstruction. They utilized prior information from images reconstructed by filtered back projection to initialize the Gaussian attributes and adopted adaptive density control (Sec. 3.2.2) to optimize all 3D Gaussians in the projection space. Note that [227] used 3D Gaussians as the basis for the volumetric representation and does not involve the splatting process.

## 6 PERFORMANCE COMPARISON

In this section, we provide more empirical evidence by presenting the performance of several 3D GS algorithms that we previously discussed. The diverse applications of 3D GS across numerous tasks, coupled with the custom-tailored algorithmic designs for each task, render a uniform comparison of all 3D GS algorithms across a single task or dataset impracticable. Therefore, drawing from our analysis

in Sec. 5, we have chosen several representative tasks within the 3D GS domain for an in-depth performance evaluation. The performance scores are primarily sourced from the original papers, except where indicated otherwise.

### 6.1 Performance Benchmarking: Localization

The localization task in SLAM involves determining the precise position and orientation of a robot or device within an environment, typically using sensor data.

- **Dataset:** Replica [193] dataset is a collection of 18 highly detailed 3D indoor scenes. These scenes are not only visually realistic but also offer comprehensive data including dense meshes, high-quality HDR textures, and detailed semantic information for each element. Following [195], three sequences about rooms and five sequences about offices are used for the evaluation.

- **Benchmarking Algorithms:** For performance comparison, we involve four recent papers which introduce 3D Gaussians into their systems [116]–[119], as well as seven typical SLAM methods [194]–[200]

- **Evaluation Metric:** The root mean square error (RMSE) of the absolute trajectory error (ATE) is a commonly used metric in evaluating SLAM systems [228], which measures the root mean square of the Euclidean distances between the estimated and true positions over the entire trajectory of the robot or device.

- **Result:** As shown in Table 1, the recent 3D Gaussians based localization algorithms have a clear advantage over existing NeRF based dense visual SLAM. For example, SplaTAM [119] achieves a trajectory error improvement of over 30%, decreasing it from 0.52cm to **0.36cm** compared to the previous state-of-the-art (SOTA) [199]. We attribute this to the dense and accurate 3D Gaussians reconstructed for scenes, which can handle the noise of real sensors. This reveals that effective scene representations can improve the accuracy of localization tasks.

### 6.2 Performance Benchmarking: Rendering Quality in Static Scenes

Rendering focuses on transforming computer-readable information (*e.g.*, 3D objects in the scene) to pixel-based images. This section focuses on evaluating the quality of rendering results in static scenes.

TABLE 2

**Quantitative rendering results (§6.2)** on Replica [193], in terms of PSNR, SSIM, and LPIPS. The numbers of FPS are taken from [116].

Method	GS	Metric	Room0	Room1	Room2	Office0	Office1	Office2	Office3	Office4	Avarage	FPS
NICE-SLAM [197] <sub>[CVPR22]</sub>		PSNR↑	22.12	22.47	24.52	29.07	30.34	19.66	22.23	24.94	24.42	0.54
		SSIM↑	0.69	0.76	0.81	0.87	0.89	0.80	0.80	0.86	0.81	
		LPIPS↓	0.33	0.27	0.21	0.23	0.18	0.23	0.21	0.20	0.23	
Vox-Fusion [196] <sub>[ISMAR22]</sub>		PSNR↑	22.39	22.36	23.92	27.79	29.83	20.33	23.47	25.21	24.41	2.17
		SSIM↑	0.68	0.75	0.80	0.86	0.88	0.79	0.80	0.85	0.80	
		LPIPS↓	0.30	0.27	0.23	0.24	0.18	0.24	0.21	0.20	0.24	
Point-SLAM [199] <sub>[ICCV23]</sub>		PSNR↑	32.40	34.08	35.50	38.26	39.16	33.99	33.48	33.49	35.17	1.33
		SSIM↑	0.97	0.98	0.98	0.98	0.99	0.96	0.96	0.98	0.97	
		LPIPS↓	0.11	0.12	0.11	0.10	0.12	0.16	0.13	0.14	0.12	
Gaussian-SLAM [117] <sub>[arXiv]</sub>	✓	PSNR↑	34.31	37.28	38.18	43.97	43.56	37.39	36.48	40.19	38.90	-
		SSIM↑	0.99	0.99	0.99	1.00	0.99	0.99	0.99	1.00	0.99	
		LPIPS↓	0.08	0.07	0.07	0.04	0.07	0.08	0.08	0.07	0.07	
GSSLAM [116] <sub>[CVPR24]</sub>	✓	PSNR↑	34.83	36.43	37.49	39.95	42.09	36.24	36.70	36.07	37.50	769
		SSIM↑	0.95	0.96	0.96	0.97	0.98	0.96	0.96	0.96	0.96	
		LPIPS↓	0.07	0.08	0.07	0.07	0.06	0.08	0.07	0.10	0.07	
SplaTAM [119] <sub>[CVPR24]</sub>	✓	PSNR↑	32.86	33.89	35.25	38.26	39.17	31.97	29.70	31.81	34.11	-
		SSIM↑	0.98	0.97	0.98	0.98	0.98	0.97	0.95	0.95	0.97	
		LPIPS↓	0.07	0.10	0.08	0.09	0.09	0.10	0.12	0.15	0.10	
GS-SLAM [118] <sub>[CVPR24]</sub>	✓	PSNR↑	31.56	32.86	32.59	38.70	41.17	32.36	32.03	32.92	34.27	-
		SSIM↑	0.97	0.97	0.97	0.99	0.99	0.98	0.97	0.97	0.97	
		LPIPS↓	0.09	0.07	0.09	0.05	0.03	0.09	0.11	0.11	0.08	

TABLE 3

**Quantitative rendering results (§6.3)** on D-NeRF [122], in terms of PSNR, SSIM, and LPIPS. \* denotes numbers taken from [99].

Method	GS	PSNR↑	SSIM↑	LPIPS↓
D-NeRF [122] <sub>[CVPR21]</sub>		30.50	0.95	0.07
TiNeuVox-B [229] <sub>[SGA22]</sub>		32.67	0.97	0.04
KPlanes [37] <sub>[CVPR23]</sub>		31.61	0.97	-
HexPlane-Slim [230] <sub>[CVPR23]</sub>		32.68	0.97	0.02
FFDNeRF [125] <sub>[ICCV23]</sub>		32.68	0.97	0.02
MSTH [231] <sub>[NeurIPS23]</sub>		31.34	0.98	0.02
3D GS* [12] <sub>[TOG23]</sub>	✓	23.19	0.93	0.08
4DGS [97] <sub>[ICLR24]</sub>	✓	34.09	0.98	-
CoGS [133] <sub>[CVPR24]</sub>	✓	37.90	0.98	0.02
4D-GS [99] <sub>[CVPR24]</sub>	✓	34.05	0.98	0.02
D-3DGS [98] <sub>[CVPR24]</sub>	✓	39.51	0.99	0.01

• **Dataset:** The same dataset as in Sec. 6.1, *i.e.*, Replica [193], is used for performance comparison.

• **Benchmarking Algorithms:** For performance comparison, we involve four recent papers which introduce 3D Gaussians into their systems [116]–[119], as well as three dense SLAM methods [196], [197], [199].

• **Evaluation Metric:** Peak signal-to-noise ratio (PSNR), structural similarity (SSIM) [232], and learned perceptual image patch similarity (LPIPS) [233] are used for measuring RGB rendering performance.

• **Result:** Table 2 shows that 3D Gaussians based systems generally outperform the three dense SLAM competitors. For example, Gaussian-SLAM [117] establishes new SOTA and outperforms previous methods by a large margin. Compared to Point-SLAM [199], GSSLAM [116] is about 578 times faster in achieving very competitive accuracy. In contrast to previous method [199] that relies on depth information, such as depth-guided ray sampling, for synthesizing novel views, 3D GS based system [116] eliminates this need, allowing for efficient rendering for any given views with high fidelity.

### 6.3 Performance Benchmarking: Rendering Quality in Dynamic Scenes

This section focuses on evaluating the rendering quality in dynamic scenes.

• **Dataset:** D-NeRF [122] dataset includes videos with 50 to 200 frames each, captured from unique viewpoints. It features synthetic, animated objects in complex scenes, with non-Lambertian materials. The dataset provides 50 to 200 training images and 20 test images per scene, designed for evaluating models in monocular settings with varied camera poses.

• **Benchmarking Algorithms:** For performance comparison, we involve four recent papers that model dynamic scenes with 3D GS [97], [99], [133], [134], as well as six NeRF based approaches [37], [122], [125], [229]–[231].

• **Evaluation Metric:** The same metrics as in Sec. 6.2, *i.e.*, PSNR, SSIM [232], and LPIPS [233], are used for evaluation.

• **Result:** From Table 3 we can observe that 3D GS based methods outperform existing SOTAs by a clear margin. The static version of 3D GS [12] fails to reconstruct dynamic scenes, resulting in a sharp drop in performance. By modeling the dynamics, CoGS [133] outperforms the SOTA method, FFDNeRF [125], by 5.22dB in terms of PSNR. These impressive results indicate the effectiveness of introducing additional properties or structured information to model the deformation of 3D Gaussians so as to model the scene dynamics.

### 6.4 Performance Benchmarking: Rendering Quality in Driving Scenes

This section focuses on evaluating the rendering quality in driving scenes, which is essential for autonomous driving.

• **Dataset:** nuScenes [204] dataset is a comprehensive collection for autonomous driving research, featuring 1000 driving scenes captured using an array of sensors including six cameras, one LiDAR, five RADARs, GPS, and IMU. It provides detailed annotations for 23 object classes with 3D bounding boxes. Six challenging scenes are used for evaluation [213].

TABLE 4

**Quantitative rendering results** (§6.4) on nuScenes [204], in terms of PSNR, SSIM, and LPIPS. \* denotes numbers taken from [213].

Method	GS	PSNR $\uparrow$	SSIM $\uparrow$	LPIPS $\downarrow$
Mip-NeRF [234] [ICCV21]		18.08	0.57	0.55
Mip-NeRF 360 [10] [CVPR22]		22.61	0.69	0.40
Instant-NGP [11] [TOG22]		16.78	0.52	0.57
Urban-NeRF [235] [CVPR22]		20.75	0.63	0.48
S-NeRF [236] [ICLR23]		25.43	0.73	0.30
SUDS [237] [CVPR23]		21.26	0.60	0.47
3D GS* [12] [TOG23]	✓	26.08	0.72	0.30
DrivingGaussian-S [213] [CVPR24]	✓	28.36	0.85	0.26
DrivingGaussian-L [213] [CVPR24]	✓	28.74	0.86	0.24

TABLE 5

**Quantitative avatar modeling results** (§6.5) on ZJU-MoCap [238], in terms of PSNR, SSIM, and LPIPS\*. The numbers of non-GS methods and FPS are taken from [164] and [182], respectively. † denotes the average of the values reported in the original paper.

Method	GS	PSNR $\uparrow$	SSIM $\uparrow$	LPIPS* $\downarrow$	FPS
NeuralBody [238] [CVPR21]		29.03	0.96	42.47	3.5
AnimNeRF [239] [ICCV21]		29.77	0.96	46.89	2.1
PixelNeRF [240] [ICCV21]		24.71	0.89	121.86	-
NHP [241] [NeurIPS21]		28.25	0.95	64.77	-
HumanNeRF [242] [CVPR22]		30.66	0.97	33.38	0.4
Instant-NVR [243] [CVPR23]		31.01	0.97	38.45	1.5
Human101 [182] [arXiv]	✓	31.79	0.96	35.75	104.0
HUGS† [166] [CVPR24]	✓	30.98	0.97	26.67	-
3DGS-Avatar† [179] [CVPR24]	✓	30.61	0.97	29.58	-
GART [164] [CVPR24]	✓	32.22	0.98	29.21	-

- **Benchmarking Algorithms:** For performance comparison, we involve one recent paper which models driving scene with 3D GS [213], as well as six NeRF based approaches [10], [11], [234]–[237].

- **Evaluation Metric:** PSNR, SSIM [232], and LPIPS [233] are used for evaluation.

- **Result:** The results in Table 4 demonstrate that the 3D GS based methods significantly surpass the NeRF based methods across all evaluated metrics. For instance, DrivingGaussian-L [213] outperforms S-NeRF [236] by 3.31dB in terms of PSNR. This suggests that 3D Gaussians can benefit from multi-sensor information to capture dynamic objects in driving scenes, especially fast-moving dynamic objects.

## 6.5 Performance Benchmarking: Human Avatar

Human avatar modeling aims to create the model of human avatars from a given multi-view video.

- **Dataset:** ZJU-MoCap [238] dataset is a prevalent benchmark in human modeling from videos, captured with 23 synchronized cameras at a 1024×1024 resolution. Following [242], six subjects (*i.e.*, 377, 386, 387, 392, 393, and 394) are used for evaluation.

- **Benchmarking Algorithms:** For performance comparison, we involve four recent papers which model human avatar with 3D GS [164], [166], [179], [182], as well as six human rendering approaches [238]–[243].

- **Evaluation Metric:** PSNR, SSIM [232], and LPIPS\* [233] are used for measuring RGB rendering performance. Here LPIPS\* equals to LPIPS × 1000.

- **Result:** Table 5 presents the numerical results of top-leading solutions in human avatar modeling. We observe

TABLE 6

**Quantitative surgical 3D reconstruction results** (§6.6) on EndoNeRF [216], in terms of PSNR, SSIM, and LPIPS. The numbers of non-GS methods and FPS are taken from [220]. † denotes the average of the values reported in the original paper.

Method	GS	PSNR $\uparrow$	SSIM $\uparrow$	LPIPS $\downarrow$	FPS $\uparrow$	Mem. $\downarrow$
EndoNeRF [216] [MICCAI22]		36.06	0.93	0.09	0.04	19GB
EndoSurf [218] [MICCAI23]		36.53	0.95	0.07	0.04	17GB
LerPlane-9k [217] [MICCAI23]		35.00	0.93	0.08	0.91	20GB
LerPlane-32k [217] [MICCAI23]		37.38	0.95	0.05	0.87	20GB
Endo-4DGS† [219] [arXiv]	✓	37.00	0.96	0.05	-	4GB
EndoGaussian [220] [arXiv]	✓	37.85	0.96	0.05	195.09	2GB
EndoGS [221] [arXiv]	✓	37.94	0.97	0.03	-	-

that introducing 3D GS into the framework leads to consistent performance improvements in both rendering quality and speed. For instance, GART [164] outperforms current SOTA, Instant-NVR [243], by 1.21dB in terms of PSNR. Note that Human101 [182] is about 68 times faster in achieving very competitive accuracy compared to Instant-NVR [243]. Considering the enhanced fidelity, inference speed and editability, 3D GS based avatar modeling may revolutionize the field of 3D animation, interactive gaming, *etc.*

## 6.6 Performance Benchmarking: Surgical 3D Reconstruction

3D reconstruction from endoscopic video is critical to robotic-assisted minimally invasive surgery, enabling pre-operative planning, training through AR/VR simulations, and intraoperative guidance.

- **Dataset:** EndoNeRF [216] dataset presents a specialized collection of stereo camera captures, comprising two samples of in-vivo prostatectomy. It is tailored to represent real-world surgical complexities, including challenging scenes with tool occlusion and pronounced non-rigid deformation.

- **Benchmarking Algorithms:** For performance comparison, we involve three recent papers which reconstruct dynamic 3D endoscopic scenes with GS [219]–[221], as well as three NeRF-based surgical reconstruction approaches [216]–[218].

- **Evaluation Metric:** PSNR, SSIM [232], and LPIPS [233] are adopted for evaluation. In addition, the requirement for GPU memory is also reported.

- **Result:** Table 6 shows that introducing the explicit representation of 3D Gaussians leads to several significant improvements. For instance, EndoGaussian [220] outperforms a strong baseline, LerPlane-32k [217], among all metrics. In particular, EndoGaussian demonstrates an approximate 224-fold increase in speed while consumes just 10% of the GPU resources. These impressive results attest to the efficiency of GS-based methods, which not only expedite processing but also minimize GPU load, thus easing the demands on hardware. Such attributes are vitally significant for real-world surgical application deployment, where optimized resource usage can be a crucial determinant of practical utility.

## 7 FUTURE RESEARCH DIRECTIONS

As impressive as those follow-up works on 3D GS are, and as much as those fields have been or might be revolutionized by 3D GS, there is a general agreement that 3D GS still has considerable room for improvement.

• **Physics- and Semantics-aware Scene Representation.** As a new, explicit scene representation technique, 3D Gaussian offers transformative potential beyond merely enhancing novel-view synthesis. It has the potential to pave the way for simultaneous advancements in scene reconstruction and understanding by devising physics- and semantics-aware 3D GS systems. This is poised to revolutionize a range of fields and downstream applications. For instance, incorporating prior knowledge such as the general shape of objects can reduce the need for extensive training viewpoints [54], [55] while improving geometry/surface reconstruction [82], [244]. A critical metric for assessing scene representation is the realism of its generated scenes, which encompasses challenges in geometry, texture, and lighting fidelity [70], [131], [186]. By merging physical principles and semantic information within the 3D GS framework, one can expect that the realism will be enhanced, thereby facilitating dynamics modeling [25], [245], editing [94], [96], generation [142], [143], and beyond. In a nutshell, pursuing this advanced and versatile scene representation opens up new possibilities for innovation in computational creativity and practical applications across diverse domains.

• **3D GS for Robotics.** In the world of robotics, especially when it comes to robots performing tasks that involve handling objects in ways similar to humans, there is a growing need for these machines to be able to navigate and manipulate their environment in a more intuitive and dynamic manner. This necessity stems from the desire to deploy intelligent robots in real-world settings, where they are often faced with new and unfamiliar tasks. Traditional approaches to robotic manipulation have relied heavily on understanding the environment through semantic representation, which means identifying objects and their attributes. However, these methods often overlook the importance of how things move and interact over time, which is crucial for completing tasks in the way humans intend. Imagine a robot trying to stack blocks based on a verbal command. Using only semantic representation, the robot might recognize the blocks but fail to stack them if it does not understand how the blocks should be positioned and moved relative to each other over time. This gap in understanding can lead to failure in executing tasks that require interaction with multiple objects or navigating dynamic environments. Due to its explicit nature, 3D GS can be used beyond mere semantic and structural analysis of environments; it also encompasses the dynamic aspect, providing a comprehensive understanding of how scenes evolve and objects interact over time. This is essential for robots tasked with navigating and manipulating their surroundings. Although initial efforts [246], [247] to construct world models using 3D GS are promising, they represent only the beginning of what is possible. Further research in this area is anticipated to enhance the capabilities of robots in performing tasks that require an understanding of both the physical space and the temporal changes within it.

• **Modeling Internal Structures of Objects with 3D GS.** Despite the ability of 3D GS to produce highly realistic renderings, modeling internal structures of objects (*e.g.*, for a scanned object in computed tomography) within the current GS framework presents a notable challenge. Due to the splatting and density control process, the current repre-

sentation of 3D Gaussian is unorganized and cannot align well with the object's actual internal structures. Moreover, there is a strong preference in various applications to depict objects as volumes (*e.g.*, computed tomography). However, the disordered nature of 3D GS makes volume modeling particularly difficult. Li *et al.* [227] used 3D Gaussians with density control as the basis for the volumetric representation and did not involve the splatting process. X-Gaussian [226] involves the splatting process for fast training and inference but cannot generate volumetric representation. Using 3D GS to model the internal structures of objects remains unanswered and deserves further exploration.

• **3D Large-scale Scene Reconstruction.** 3D scene reconstruction and rendering, particularly for large-scale environments, has garnered considerable interest due to its applications in various fields, such as AR, VR, and autonomous driving. It is impractical to use 3D GS directly for large-scale scene reconstruction due to: *i*) reconstructing large-scale scenes within the current framework is unfeasible for the hardware; and *ii*) rendering so many Gaussians introduces a substantial computational load. As an early attempt, CityGS [248] proposes a divide-and-conquer training strategy alongside a level-of-detail rendering approach, by partitioning a large scene into smaller, manageable blocks, each represented by a reduced number of Gaussians. Overall, reconstructing large-scale scenes using 3D GS still holds significant potential waiting to be explored.

• **3D GS for Simulation in Autonomous Driving.** Collecting real-world datasets for autonomous driving is both expensive and logistically challenging, yet crucial for training effective image-based perception systems. To mitigate these issues, simulation emerges as a cost-effective alternative, enabling the generation of synthetic datasets across diverse environments. However, the development of simulators capable of producing realistic and diverse synthetic data is fraught with challenges. These include achieving a high level of realism, accommodating various control methods, and accurately simulating a range of lighting conditions. While early efforts [213]–[215] in reconstructing urban/street scenes with 3D GS have been encouraging, they are just the tip of the iceberg in terms of the full capabilities. There remain numerous critical aspects to be explored, such as the integration of user-defined object models, the modeling of physics-aware scene changes (*e.g.*, the rotation of vehicle wheels), and the enhancement of controllability and realism (*e.g.*, in varying lighting conditions).

• **Empowering 3D GS with More Possibilities.** Despite the significant potential of 3D GS, the full scope of applications for 3D GS remains largely untapped. A promising avenue for exploration involves augmenting 3D Gaussians with additional attributes (*e.g.*, linguistic and spatiotemporal properties as mentioned in Sec. 4.5) and introducing structured information (*e.g.*, spatial MLPs and grids as mentioned in Sec. 4.6), tailored for specific applications. Moreover, recent studies have begun to unveil the capability of 3D GS in several domains, *e.g.*, camera pose estimation [249], the capture of hand-object interactions [250], the quantification of uncertainty [251], surgical scene reconstruction [219]–[221], and fluid synthesis [252]. These preliminary findings highlight a significant opportunity for interdisciplinary scholars to explore 3D GS further.

## 8 CONCLUSIONS

To the best of our knowledge, this survey presents the first comprehensive overview of 3D GS, a groundbreaking technique revolutionizing explicit radiance fields, computer graphics, and computer vision. It delineates the paradigm shift from traditional NeRF based methods, spotlighting the advantages of 3D GS in real-time rendering and enhanced editability. Our detailed analysis demonstrates the superiority of 3D GS in practical applications, particularly those highly sensitive to latency. We offer insights into principles, prospective research directions, and the unresolved challenges within this domain. Overall, 3D GS stands as a transformative technology, poised to significantly influence future advancements in 3D reconstruction and representation. This survey is intended to serve as a foundational resource, propelling further exploration and progress in this rapidly evolving field.

## REFERENCES

- [1] S. J. Gortler, R. Grzeszczuk, R. Szeliski, and M. F. Cohen, "The lumigraph," in *Seminal Graphics Papers: Pushing the Boundaries, Volume 2*, 2023, pp. 453–464.
- [2] M. Levoy and P. Hanrahan, "Light field rendering," in *Seminal Graphics Papers: Pushing the Boundaries, Volume 2*, 2023, pp. 441–452.
- [3] C. Buehler, M. Bosse, L. McMillan, S. Gortler, and M. Cohen, "Unstructured lumigraph rendering," in *Seminal Graphics Papers: Pushing the Boundaries, Volume 2*, 2023, pp. 497–504.
- [4] N. Snavely, S. M. Seitz, and R. Szeliski, "Photo tourism: exploring photo collections in 3d," in *ACM TOG*, 2006, pp. 835–846.
- [5] M. Goesele, N. Snavely, B. Curless, H. Hoppe, and S. M. Seitz, "Multi-view stereo for community photo collections," in *ICCV*, 2007, pp. 1–8.
- [6] A. Chen, Z. Xu, A. Geiger, J. Yu, and H. Su, "Tensorf: Tensorial radiance fields," in *European Conference on Computer Vision*, 2022, pp. 333–350.
- [7] S. J. Garbin, M. Kowalski, M. Johnson, J. Shotton, and J. Valentin, "Fastnerf: High-fidelity neural rendering at 200fps," in *ICCV*, 2021, pp. 14 346–14 355.
- [8] C. Reiser, S. Peng, Y. Liao, and A. Geiger, "Kilonerf: Speeding up neural radiance fields with thousands of tiny mlps," in *ICCV*, 2021, pp. 14 335–14 345.
- [9] T. Takikawa, J. Litalien, K. Yin, K. Kreis, C. Loop, D. Nowrouzezahrai, A. Jacobson, M. McGuire, and S. Fidler, "Neural geometric level of detail: Real-time rendering with implicit 3d shapes," in *CVPR*, 2021, pp. 11 358–11 367.
- [10] J. T. Barron, B. Mildenhall, D. Verbin, P. P. Srinivasan, and P. Hedman, "Mip-nerf 360: Unbounded anti-aliased neural radiance fields," in *CVPR*, 2022, pp. 5470–5479.
- [11] T. Müller, A. Evans, C. Schied, and A. Keller, "Instant neural graphics primitives with a multiresolution hash encoding," *ACM TOG*, vol. 41, no. 4, pp. 1–15, 2022.
- [12] B. Kerbl, G. Kopanas, T. Leimkühler, and G. Drettakis, "3d gaussian splatting for real-time radiance field rendering," *ACM TOG*, vol. 42, no. 4, 2023.
- [13] P. Henzler, N. J. Mitra, and T. Ritschel, "Escaping plato's cave: 3d shape from adversarial rendering," in *ICCV*, 2019, pp. 9984–9993.
- [14] V. Sitzmann, J. Thies, F. Heide, M. Nießner, G. Wetzstein, and M. Zollhofer, "Deepvoxels: Learning persistent 3d feature embeddings," in *CVPR*, 2019, pp. 2437–2446.
- [15] B. Mildenhall, P. P. Srinivasan, M. Tancik, J. T. Barron, R. Ramamoorthi, and R. Ng, "Nerf: Representing scenes as neural radiance fields for view synthesis," in *ECCV*, 2020, pp. 405–421.
- [16] H. Pfister, M. Zwicker, J. Van Baar, and M. Gross, "Surfels: Surface elements as rendering primitives," in *Proceedings of the 27th annual conference on Computer graphics and interactive techniques*, 2000, pp. 335–342.
- [17] M. Zwicker, H. Pfister, J. Van Baar, and M. Gross, "Surface splatting," in *Proceedings of the 28th annual conference on Computer graphics and interactive techniques*, 2001, pp. 371–378.
- [18] L. Ren, H. Pfister, and M. Zwicker, "Object space ewa surface splatting: A hardware accelerated approach to high quality point rendering," in *Computer Graphics Forum*, no. 3, 2002, pp. 461–470.
- [19] M. Botsch, A. Hornung, M. Zwicker, and L. Kobbelt, "High-quality surface splatting on today's gpus," in *Proceedings Eurographics/IEEE VGTC Symposium Point-Based Graphics, 2005.*, 2005, pp. 17–141.
- [20] W. Yifan, F. Serena, S. Wu, C. Öztireli, and O. Sorkine-Hornung, "Differentiable surface splatting for point-based geometry processing," *ACM TOG*, vol. 38, no. 6, pp. 1–14, 2019.
- [21] O. Wiles, G. Gkioxari, R. Szeliski, and J. Johnson, "Synsin: End-to-end view synthesis from a single image," in *CVPR*, 2020, pp. 7467–7477.
- [22] D. Kalkofen, E. Mendez, and D. Schmalstieg, "Comprehensible visualization for augmented reality," *IEEE TVCG*, vol. 15, no. 2, pp. 193–204, 2008.
- [23] A. Patney, M. Salvi, J. Kim, A. Kaplanyan, C. Wyman, N. Benty, D. Luebke, and A. Lefohn, "Towards foveated rendering for gaze-tracked virtual reality," *ACM TOG*, vol. 35, no. 6, pp. 1–12, 2016.
- [24] R. Albert, A. Patney, D. Luebke, and J. Kim, "Latency requirements for foveated rendering in virtual reality," *ACM Transactions on Applied Perception (TAP)*, vol. 14, no. 4, pp. 1–13, 2017.
- [25] Y. Jiang, C. Yu, T. Xie, X. Li, Y. Feng, H. Wang, M. Li, H. Lau, F. Gao, Y. Yang *et al.*, "Vr-gs: A physical dynamics-aware interactive gaussian splatting system in virtual reality," *arXiv preprint arXiv:2401.16663*, 2024.
- [26] R. Chabra, J. E. Lenssen, E. Ilg, T. Schmidt, J. Straub, S. Lovegrove, and R. Newcombe, "Deep local shapes: Learning local sdf priors for detailed 3d reconstruction," in *ECCV*, 2020, pp. 608–625.
- [27] Z. Wang, J. Phillion, S. Fidler, and J. Kautz, "Learning indoor inverse rendering with 3d spatially-varying lighting," in *ICCV*, 2021, pp. 12 538–12 547.
- [28] C. Sun, M. Sun, and H.-T. Chen, "Direct voxel grid optimization: Super-fast convergence for radiance fields reconstruction," in *CVPR*, 2022, pp. 5459–5469.
- [29] L. Kobbelt and M. Botsch, "A survey of point-based techniques in computer graphics," *Computers & Graphics*, vol. 28, no. 6, pp. 801–814, 2004.
- [30] Y. Xie, T. Takikawa, S. Saito, O. Litany, S. Yan, N. Khan, F. Tombari, J. Tompkin, V. Sitzmann, and S. Sridhar, "Neural fields in visual computing and beyond," in *Computer Graphics Forum*, no. 2, 2022, pp. 641–676.
- [31] A. Tewari, J. Thies, B. Mildenhall, P. Srinivasan, E. Tretschk, W. Yifan, C. Lassner, V. Sitzmann, R. Martin-Brualla, S. Lombardi *et al.*, "Advances in neural rendering," in *Computer Graphics Forum*, no. 2, 2022, pp. 703–735.
- [32] X.-F. Han, H. Laga, and M. Bannamoun, "Image-based 3d object reconstruction: State-of-the-art and trends in the deep learning era," *IEEE TPAMI*, vol. 43, no. 5, pp. 1578–1604, 2019.
- [33] J. Yuan, T. Chen, B. Li, and X. Xue, "Compositional scene representation learning via reconstruction: A survey," *IEEE TPAMI*, 2023.
- [34] W. Wang, Y. Yang, and Y. Pan, "Visual knowledge in the big model era: Retrospect and prospect," *arXiv preprint arXiv:2404.04308*, 2024.
- [35] L. Mescheder, M. Oechsle, M. Niemeyer, S. Nowozin, and A. Geiger, "Occupancy networks: Learning 3d reconstruction in function space," in *CVPR*, 2019, pp. 4460–4470.
- [36] J. J. Park, P. Florence, J. Straub, R. Newcombe, and S. Lovegrove, "Deepsdf: Learning continuous signed distance functions for shape representation," in *CVPR*, 2019, pp. 165–174.
- [37] S. Fridovich-Keil, G. Meanti, F. R. Warburg, B. Recht, and A. Kanazawa, "K-planes: Explicit radiance fields in space, time, and appearance," in *CVPR*, 2023, pp. 12 479–12 488.
- [38] M. Eisemann, B. De Decker, M. Magnor, P. Bekaert, E. De Aguiar, N. Ahmed, C. Theobalt, and A. Sellent, "Floating textures," in *Computer graphics forum*, no. 2, 2008, pp. 409–418.
- [39] G. Chaurasia, S. Duchene, O. Sorkine-Hornung, and G. Drettakis, "Depth synthesis and local warps for plausible image-based navigation," *ACM TOG*, vol. 32, no. 3, pp. 1–12, 2013.
- [40] P. Hedman, J. Philip, T. Price, J.-M. Frahm, G. Drettakis, and G. Brostow, "Deep blending for free-viewpoint image-based rendering," *ACM TOG*, vol. 37, no. 6, pp. 1–15, 2018.
- [41] G. Kopanas, J. Philip, T. Leimkühler, and G. Drettakis, "Point-based neural rendering with per-view optimization," in *Computer Graphics Forum*, no. 4, 2021, pp. 29–43.

- [42] J. Flynn, I. Neulander, J. Philbin, and N. Snavely, "Deepstereo: Learning to predict new views from the world's imagery," in *CVPR*, 2016, pp. 5515–5524.
- [43] T. Zhou, S. Tulsiani, W. Sun, J. Malik, and A. A. Efros, "View synthesis by appearance flow," in *ECCV*, 2016, pp. 286–301.
- [44] J. Thies, M. Zollhöfer, and M. Nießner, "Deferred neural rendering: Image synthesis using neural textures," *ACM TOG*, vol. 38, no. 4, pp. 1–12, 2019.
- [45] G. Riegler and V. Koltun, "Free view synthesis," in *ECCV*, 2020, pp. 623–640.
- [46] E. Penner and L. Zhang, "Soft 3d reconstruction for view synthesis," *ACM TOG*, vol. 36, no. 6, pp. 1–11, 2017.
- [47] K.-A. Aliev, A. Sevastopolsky, M. Kolos, D. Ulyanov, and V. Lempitsky, "Neural point-based graphics," in *ECCV*, 2020, pp. 696–712.
- [48] D. Rückert, L. Franke, and M. Stamminger, "Adop: Approximate differentiable one-pixel point rendering," *ACM TOG*, vol. 41, no. 4, pp. 1–14, 2022.
- [49] S. Laine and T. Karras, "High-performance software rasterization on gpus," in *Proceedings of the ACM SIGGRAPH Symposium on High Performance Graphics*, 2011, pp. 79–88.
- [50] M. Schütz, B. Kerbl, and M. Wimmer, "Software rasterization of 2 billion points in real time," *Proceedings of the ACM on Computer Graphics and Interactive Techniques*, vol. 5, no. 3, pp. 1–17, 2022.
- [51] M. Zwicker, H. Pfister, J. Van Baar, and M. Gross, "Ewa volume splatting," in *Proceedings Visualization, 2001. VIS'01.*, 2001, pp. 29–538.
- [52] H. Xiong, S. Muttukuru, R. Upadhyay, P. Chari, and A. Kadambi, "Sparsegs: Real-time 360  $\{\backslash\deg\}$  sparse view synthesis using gaussian splatting," *arXiv preprint arXiv:2312.00206*, 2023.
- [53] Z. Zhu, Z. Fan, Y. Jiang, and Z. Wang, "Fsgs: Real-time few-shot view synthesis using gaussian splatting," *arXiv preprint arXiv:2312.00451*, 2023.
- [54] D. Charatan, S. Li, A. Tagliasacchi, and V. Sitzmann, "pixelsplat: 3d gaussian splats from image pairs for scalable generalizable 3d reconstruction," *arXiv preprint arXiv:2312.12337*, 2023.
- [55] S. Szymanowicz, C. Rupprecht, and A. Vedaldi, "Splatter image: Ultra-fast single-view 3d reconstruction," *arXiv preprint arXiv:2312.13150*, 2023.
- [56] J. Li, J. Zhang, X. Bai, J. Zheng, X. Ning, J. Zhou, and L. Gu, "Dngaussian: Optimizing sparse-view 3d gaussian radiance fields with global-local depth normalization," *arXiv preprint arXiv:2403.06912*, 2024.
- [57] A. Swann, M. Strong, W. K. Do, G. S. Camps, M. Schwager, and M. Kennedy III, "Touch-gs: Visual-tactile supervised 3d gaussian splatting," *arXiv preprint arXiv:2403.09875*, 2024.
- [58] Y. Chen, H. Xu, C. Zheng, B. Zhuang, M. Pollefeys, A. Geiger, T.-J. Cham, and J. Cai, "Mvsplat: Efficient 3d gaussian splatting from sparse multi-view images," *arXiv preprint arXiv:2403.14627*, 2024.
- [59] C. Wewer, K. Raj, E. Ilg, B. Schiele, and J. E. Lenssen, "latentsplat: Autoencoding variational gaussians for fast generalizable 3d reconstruction," *arXiv preprint arXiv:2403.16292*, 2024.
- [60] Y. Xu, Z. Shi, W. Yifan, H. Chen, C. Yang, S. Peng, Y. Shen, and G. Wetzstein, "Grm: Large gaussian reconstruction model for efficient 3d reconstruction and generation," *arXiv preprint arXiv:2403.14621*, 2024.
- [61] Q. Shen, X. Yi, Z. Wu, P. Zhou, H. Zhang, S. Yan, and X. Wang, "Gamba: Marry gaussian splatting with mamba for single view 3d reconstruction," *arXiv preprint arXiv:2403.18795*, 2024.
- [62] Z. Fan, K. Wang, K. Wen, Z. Zhu, D. Xu, and Z. Wang, "Light-gaussian: Unbounded 3d gaussian compression with 15x reduction and 200+ fps," *arXiv preprint arXiv:2311.17245*, 2023.
- [63] K. Navaneet, K. P. Meibodi, S. A. Koohpayegani, and H. Pirsiavash, "Compact3d: Compressing gaussian splat radiance field models with vector quantization," *arXiv preprint arXiv:2311.18159*, 2023.
- [64] J. C. Lee, D. Rho, X. Sun, J. H. Ko, and E. Park, "Compact 3d gaussian representation for radiance field," *arXiv preprint arXiv:2311.13681*, 2023.
- [65] W. Morgenstern, F. Barthel, A. Hilsmann, and P. Eisert, "Compact 3d scene representation via self-organizing gaussian grids," *arXiv preprint arXiv:2312.13299*, 2023.
- [66] X. Zhang, X. Ge, T. Xu, D. He, Y. Wang, H. Qin, G. Lu, J. Geng, and J. Zhang, "Gaussianimage: 1000 fps image representation and compression by 2d gaussian splatting," *arXiv preprint arXiv:2403.08551*, 2024.
- [67] S. Niedermayr, J. Stumpfegger, and R. Westermann, "Compressed 3d gaussian splatting for accelerated novel view synthesis," *arXiv preprint arXiv:2401.02436*, 2024.
- [68] Y. Chen, Q. Wu, J. Cai, M. Harandi, and W. Lin, "Hac: Hash-grid assisted context for 3d gaussian splatting compression," *arXiv preprint arXiv:2403.14530*, 2024.
- [69] Z. Yu, A. Chen, B. Huang, T. Sattler, and A. Geiger, "Mip-splatting: Alias-free 3d gaussian splatting," *arXiv preprint arXiv:2311.16493*, 2023.
- [70] J. Gao, C. Gu, Y. Lin, H. Zhu, X. Cao, L. Zhang, and Y. Yao, "Relightable 3d gaussian: Real-time point cloud relighting with brdf decomposition and ray tracing," *arXiv preprint arXiv:2311.16043*, 2023.
- [71] Z. Yan, W. F. Low, Y. Chen, and G. H. Lee, "Multi-scale 3d gaussian splatting for anti-aliased rendering," *arXiv preprint arXiv:2311.17089*, 2023.
- [72] Y. Jiang, J. Tu, Y. Liu, X. Gao, X. Long, W. Wang, and Y. Ma, "Gaussianshader: 3d gaussian splatting with shading functions for reflective surfaces," *arXiv preprint arXiv:2311.17977*, 2023.
- [73] T. Lu, M. Yu, L. Xu, Y. Xiangli, L. Wang, D. Lin, and B. Dai, "Scaffold-gs: Structured 3d gaussians for view-adaptive rendering," *arXiv preprint arXiv:2312.00109*, 2023.
- [74] B. Lee, H. Lee, X. Sun, U. Ali, and E. Park, "Deblurring 3d gaussian splatting," *arXiv preprint arXiv:2401.00834*, 2024.
- [75] D. Malarz, W. Smolak, J. Tabor, S. Tadeja, and P. Spurek, "Gaussian splitting algorithm with color and opacity depended on viewing direction," *arXiv preprint arXiv:2312.13729*, 2023.
- [76] L. Bolanos, S.-Y. Su, and H. Rhodin, "Gaussian shadow casting for neural characters," *arXiv preprint arXiv:2401.06116*, 2024.
- [77] L. Radl, M. Steiner, M. Parger, A. Weinrauch, B. Kerbl, and M. Steinberger, "Stopthepop: Sorted gaussian splatting for view-consistent real-time rendering," *arXiv preprint arXiv:2402.00525*, 2024.
- [78] Z. Yang, X. Gao, Y. Sun, Y. Huang, X. Lyu, W. Zhou, S. Jiao, X. Qi, and X. Jin, "Spec-gaussian: Anisotropic view-dependent appearance for 3d gaussian splatting," *arXiv preprint arXiv:2402.15870*, 2024.
- [79] C. Peng, Y. Tang, Y. Zhou, N. Wang, X. Liu, D. Li, and R. Chellappa, "Bags: Blur agnostic gaussian splatting through multi-scale kernel modeling," *arXiv preprint arXiv:2403.04926*, 2024.
- [80] L. Zhao, P. Wang, and P. Liu, "Bad-gaussians: Bundle adjusted deblur gaussian splatting," *arXiv preprint arXiv:2403.11831*, 2024.
- [81] H. Dahmani, M. Bennehar, N. Piasco, L. Roldao, and D. Tsishkou, "Swag: Splatting in the wild images with appearance-conditioned gaussians," *arXiv preprint arXiv:2403.10427*, 2024.
- [82] Y. Li, C. Lyu, Y. Di, G. Zhai, G. H. Lee, and F. Tombari, "Geogaussian: Geometry-aware gaussian splatting for scene rendering," *arXiv preprint arXiv:2403.11324*, 2024.
- [83] Z. Liang, Q. Zhang, W. Hu, Y. Feng, L. Zhu, and K. Jia, "Analytic-splatting: Anti-aliased 3d gaussian splatting via analytic integration," *arXiv preprint arXiv:2403.11056*, 2024.
- [84] O. Seiskari, J. Ylilampi, V. Kaatrasalo, P. Rantalankila, M. Turkulainen, J. Kannala, E. Rahtu, and A. Solin, "Gaussian splatting on the move: Blur and rolling shutter compensation for natural camera motion," *arXiv preprint arXiv:2403.13327*, 2024.
- [85] X. Song, J. Zheng, S. Yuan, H.-a. Gao, J. Zhao, X. He, W. Gu, and H. Zhao, "Sa-gs: Scale-adaptive gaussian splatting for training-free anti-aliasing," *arXiv preprint arXiv:2403.19615*, 2024.
- [86] Y. Fu, S. Liu, A. Kulkarni, J. Kautz, A. A. Efros, and X. Wang, "Colmap-free 3d gaussian splatting," *arXiv preprint arXiv:2312.07504*, 2023.
- [87] J. Jung, J. Han, H. An, J. Kang, S. Park, and S. Kim, "Relaxing accurate initialization constraint for 3d gaussian splatting," *arXiv preprint arXiv:2403.09413*, 2024.
- [88] M. Yu, T. Lu, L. Xu, L. Jiang, Y. Xiangli, and B. Dai, "Gsdgs: 3dgs meets sdf for improved rendering and reconstruction," *arXiv preprint arXiv:2403.16964*, 2024.
- [89] J. Zhang, F. Zhan, M. Xu, S. Lu, and E. Xing, "Fregs: 3d gaussian splatting with progressive frequency regularization," *arXiv preprint arXiv:2403.06908*, 2024.
- [90] Q. Feng, G. Cao, H. Chen, T.-J. Mu, R. R. Martin, and S.-M. Hu, "A new split algorithm for 3d gaussian splatting," *arXiv preprint arXiv:2403.09143*, 2024.
- [91] J.-C. Shi, M. Wang, H.-B. Duan, and S.-H. Guan, "Language embedded 3d gaussians for open-vocabulary scene understanding," *arXiv preprint arXiv:2311.18482*, 2023.

- [92] M. Qin, W. Li, J. Zhou, H. Wang, and H. Pfister, "Langsplat: 3d language gaussian splatting," *arXiv preprint arXiv:2312.16084*, 2023.
- [93] X. Zuo, P. Samangouei, Y. Zhou, Y. Di, and M. Li, "Fmgs: Foundation model embedded 3d gaussian splatting for holistic 3d scene understanding," *arXiv preprint arXiv:2401.01970*, 2024.
- [94] S. Zhou, H. Chang, S. Jiang, Z. Fan, Z. Zhu, D. Xu, P. Chari, S. You, Z. Wang, and A. Kadambi, "Feature 3dgs: Supercharging 3d gaussian splatting to enable distilled feature fields," *arXiv preprint arXiv:2312.03203*, 2023.
- [95] M. Ye, M. Danelljan, F. Yu, and L. Ke, "Gaussian grouping: Segment and edit anything in 3d scenes," *arXiv preprint arXiv:2312.00732*, 2023.
- [96] J. Cen, J. Fang, C. Yang, L. Xie, X. Zhang, W. Shen, and Q. Tian, "Segment any 3d gaussians," *arXiv preprint arXiv:2312.00860*, 2023.
- [97] Z. Yang, H. Yang, Z. Pan, X. Zhu, and L. Zhang, "Real-time photorealistic dynamic scene representation and rendering with 4d gaussian splatting," in *ICLR*, 2024.
- [98] Z. Yang, X. Gao, W. Zhou, S. Jiao, Y. Zhang, and X. Jin, "Deformable 3d gaussians for high-fidelity monocular dynamic scene reconstruction," *arXiv preprint arXiv:2309.13101*, 2023.
- [99] G. Wu, T. Yi, J. Fang, L. Xie, X. Zhang, W. Wei, W. Liu, Q. Tian, and X. Wang, "4d gaussian splatting for real-time dynamic scene rendering," *arXiv preprint arXiv:2310.08528*, 2023.
- [100] Y. Xu, B. Chen, Z. Li, H. Zhang, L. Wang, Z. Zheng, and Y. Liu, "Gaussian head avatar: Ultra high-fidelity head avatar via dynamic gaussians," *arXiv preprint arXiv:2312.03029*, 2023.
- [101] A. Gu and T. Dao, "Mamba: Linear-time sequence modeling with selective state spaces," *arXiv preprint arXiv:2312.00752*, 2023.
- [102] A. Van Den Oord, O. Vinyals *et al.*, "Neural discrete representation learning," *Advances in neural information processing systems*, vol. 30, 2017.
- [103] A. Saroha, M. Gladkova, C. Curreli, T. Yenamandra, and D. Cremers, "Gaussian splatting in style," *arXiv preprint arXiv:2403.08498*, 2024.
- [104] J. A. Placed, J. Strader, H. Carrillo, N. Atanasov, V. Indelman, L. Carlone, and J. A. Castellanos, "A survey on active simultaneous localization and mapping: State of the art and new frontiers," *IEEE Transactions on Robotics*, 2023.
- [105] H. Durrant-Whyte and T. Bailey, "Simultaneous localization and mapping: part i," *IEEE robotics & automation magazine*, vol. 13, no. 2, pp. 99–110, 2006.
- [106] T. Bailey and H. Durrant-Whyte, "Simultaneous localization and mapping (slam): Part ii," *IEEE robotics & automation magazine*, vol. 13, no. 3, pp. 108–117, 2006.
- [107] R. A. Newcombe, S. Izadi, O. Hilliges, D. Molyneaux, D. Kim, A. J. Davison, P. Kohi, J. Shotton, S. Hodges, and A. Fitzgibbon, "Kinectfusion: Real-time dense surface mapping and tracking," in *2011 10th IEEE international symposium on mixed and augmented reality*, 2011, pp. 127–136.
- [108] M. Nießner, M. Zollhöfer, S. Izadi, and M. Stamminger, "Real-time 3d reconstruction at scale using voxel hashing," *ACM TOG*, vol. 32, no. 6, pp. 1–11, 2013.
- [109] R. Maier, R. Schaller, and D. Cremers, "Efficient online surface correction for real-time large-scale 3d reconstruction," *arXiv preprint arXiv:1709.03763*, 2017.
- [110] O. Kähler, V. Prisacariu, J. Valentin, and D. Murray, "Hierarchical voxel block hashing for efficient integration of depth images," *IEEE Robotics and Automation Letters*, vol. 1, no. 1, pp. 192–197, 2015.
- [111] F. Ruetz, E. Hernández, M. Pfeiffer, H. Oleynikova, M. Cox, T. Lowe, and P. Borges, "Ovpc mesh: 3d free-space representation for local ground vehicle navigation," in *2019 International Conference on Robotics and Automation (ICRA)*, 2019, pp. 8648–8654.
- [112] T. Whelan, R. F. Salas-Moreno, B. Glocker, A. J. Davison, and S. Leutenegger, "Elasticfusion: Real-time dense slam and light source estimation," *The International Journal of Robotics Research*, vol. 35, no. 14, pp. 1697–1716, 2016.
- [113] K. Wang, F. Gao, and S. Shen, "Real-time scalable dense surfel mapping," in *2019 International conference on robotics and automation (ICRA)*, 2019, pp. 6919–6925.
- [114] R. Mur-Artal and J. D. Tardós, "Orb-slam2: An open-source slam system for monocular, stereo, and rgb-d cameras," *IEEE transactions on robotics*, vol. 33, no. 5, pp. 1255–1262, 2017.
- [115] H. Huang, L. Li, H. Cheng, and S.-K. Yeung, "Photo-slam: Real-time simultaneous localization and photorealistic mapping for monocular, stereo, and rgb-d cameras," *arXiv preprint arXiv:2311.16728*, 2023.
- [116] H. Matsuki, R. Murai, P. H. Kelly, and A. J. Davison, "Gaussian splatting slam," *arXiv preprint arXiv:2312.06741*, 2023.
- [117] V. Yugay, Y. Li, T. Gevers, and M. R. Oswald, "Gaussian-slam: Photo-realistic dense slam with gaussian splatting," *arXiv preprint arXiv:2312.10070*, 2023.
- [118] C. Yan, D. Qu, D. Wang, D. Xu, Z. Wang, B. Zhao, and X. Li, "Gs-slam: Dense visual slam with 3d gaussian splatting," *arXiv preprint arXiv:2311.11700*, 2023.
- [119] N. Keetha, J. Karhade, K. M. Jatavallabhula, G. Yang, S. Scherer, D. Ramanan, and J. Luiten, "Splatam: Splat, track & map 3d gaussians for dense rgb-d slam," *arXiv preprint arXiv:2312.02126*, 2023.
- [120] S. Hong, J. He, X. Zheng, H. Wang, H. Fang, K. Liu, C. Zheng, and S. Shen, "Liv-gaussmap: Lidar-inertial-visual fusion for real-time 3d radiance field map rendering," *arXiv preprint arXiv:2401.14857*, 2024.
- [121] Y. Ji, Y. Liu, G. Xie, B. Ma, and Z. Xie, "Neds-slam: A novel neural explicit dense semantic slam framework using 3d gaussian splatting," *arXiv preprint arXiv:2403.11679*, 2024.
- [122] A. Pumarola, E. Corona, G. Pons-Moll, and F. Moreno-Noguer, "D-nerf: Neural radiance fields for dynamic scenes," in *CVPR*, 2021, pp. 10 318–10 327.
- [123] K. Park, U. Sinha, P. Hedman, J. T. Barron, S. Bouaziz, D. B. Goldman, R. Martin-Brualla, and S. M. Seitz, "Hypernerf: A higher-dimensional representation for topologically varying neural radiance fields," *arXiv preprint arXiv:2106.13228*, 2021.
- [124] K. Park, U. Sinha, J. T. Barron, S. Bouaziz, D. B. Goldman, S. M. Seitz, and R. Martin-Brualla, "Nerfies: Deformable neural radiance fields," in *ICCV*, 2021, pp. 5865–5874.
- [125] X. Guo, J. Sun, Y. Dai, G. Chen, X. Ye, X. Tan, E. Ding, Y. Zhang, and J. Wang, "Forward flow for novel view synthesis of dynamic scenes," in *ICCV*, 2023, pp. 16 022–16 033.
- [126] Y. Lin, Z. Dai, S. Zhu, and Y. Yao, "Gaussian-flow: 4d reconstruction with dynamic 3d gaussian particle," *arXiv preprint arXiv:2312.03431*, 2023.
- [127] A. Kratimenos, J. Lei, and K. Daniilidis, "Dymmf: Neural motion factorization for real-time dynamic view synthesis with 3d gaussian splatting," *arXiv preprint arXiv:2312.00112*, 2023.
- [128] D. Das, C. Wewer, R. Yunus, E. Ilg, and J. E. Lenssen, "Neural parametric gaussians for monocular non-rigid object reconstruction," *arXiv preprint arXiv:2312.01196*, 2023.
- [129] R. Shaw, J. Song, A. Moreau, M. Nazarczuk, S. Catley-Chandar, H. Dharmo, and E. Perez-Pellitero, "Swags: Sampling windows adaptively for dynamic 3d gaussian splatting," *arXiv preprint arXiv:2312.13308*, 2023.
- [130] J. Luiten, G. Kopanas, B. Leibe, and D. Ramanan, "Dynamic 3d gaussians: Tracking by persistent dynamic view synthesis," *arXiv preprint arXiv:2308.09713*, 2023.
- [131] Y.-H. Huang, Y.-T. Sun, Z. Yang, X. Lyu, Y.-P. Cao, and X. Qi, "Sc-gs: Sparse-controlled gaussian splatting for editable dynamic scenes," *arXiv preprint arXiv:2312.14937*, 2023.
- [132] R. Shao, J. Sun, C. Peng, Z. Zheng, B. Zhou, H. Zhang, and Y. Liu, "Control4d: Dynamic portrait editing by learning 4d gan from 2d diffusion-based editor," *arXiv preprint arXiv:2305.20082*, 2023.
- [133] H. Yu, J. Julin, Z. Á. Milacski, K. Niinuma, and L. A. Jeni, "Cogs: Controllable gaussian splatting," *arXiv preprint arXiv:2312.05664*, 2023.
- [134] Y. Liang, N. Khan, Z. Li, T. Nguyen-Phuoc, D. Lanman, J. Tompkin, and L. Xiao, "Gaufre: Gaussian deformation fields for real-time dynamic novel view synthesis," *arXiv preprint arXiv:2312.11458*, 2023.
- [135] K. Katsumata, D. M. Vo, and H. Nakayama, "An efficient 3d gaussian representation for monocular/multi-view dynamic scenes," *arXiv preprint arXiv:2311.12897*, 2023.
- [136] Z. Li, Z. Chen, Z. Li, and Y. Xu, "Spacetime gaussian feature splatting for real-time dynamic view synthesis," *arXiv preprint arXiv:2312.16812*, 2023.
- [137] I. Goodfellow, J. Pouget-Abadie, M. Mirza, B. Xu, D. Warde-Farley, S. Ozair, A. Courville, and Y. Bengio, "Generative adversarial networks," *Communications of the ACM*, vol. 63, no. 11, pp. 139–144, 2020.
- [138] J. Ho, A. Jain, and P. Abbeel, "Denoising diffusion probabilistic models," in *NeurIPS*, 2020, pp. 6840–6851.
- [139] L. Zhang, A. Rao, and M. Agrawala, "Adding conditional control to text-to-image diffusion models," in *ICCV*, 2023, pp. 3836–3847.



- [140] R. Rombach, A. Blattmann, D. Lorenz, P. Esser, and B. Ommer, "High-resolution image synthesis with latent diffusion models," in *CVPR*, 2022, pp. 10 684–10 695.
- [141] Z. Chen, F. Wang, and H. Liu, "Text-to-3d using gaussian splatting," *arXiv preprint arXiv:2309.16585*, 2023.
- [142] J. Tang, J. Ren, H. Zhou, Z. Liu, and G. Zeng, "Dreamgaussian: Generative gaussian splatting for efficient 3d content creation," in *ICLR*, 2024.
- [143] T. Yi, J. Fang, G. Wu, L. Xie, X. Zhang, W. Liu, Q. Tian, and X. Wang, "Gaussiandreamer: Fast generation from text to 3d gaussian splatting with point cloud priors," *arXiv preprint arXiv:2310.08529*, 2023.
- [144] X. Li, H. Wang, and K.-K. Tseng, "Gaussiandiffusion: 3d gaussian splatting for denoising diffusion probabilistic models with structured noise," *arXiv preprint arXiv:2311.11221*, 2023.
- [145] Y. Liang, X. Yang, J. Lin, H. Li, X. Xu, and Y. Chen, "Lucidreamer: Towards high-fidelity text-to-3d generation via interval score matching," *arXiv preprint arXiv:2311.11284*, 2023.
- [146] J. Chung, S. Lee, H. Nam, J. Lee, and K. M. Lee, "Luciddreamer: Domain-free generation of 3d gaussian splatting scenes," *arXiv preprint arXiv:2311.13384*, 2023.
- [147] X. Liu, X. Zhan, J. Tang, Y. Shan, G. Zeng, D. Lin, X. Liu, and Z. Liu, "Humangaussian: Text-driven 3d human generation with gaussian splatting," *arXiv preprint arXiv:2311.17061*, 2023.
- [148] A. Vilesov, P. Chari, and A. Kadambi, "Cg3d: Compositional generation for text-to-3d via gaussian splatting," *arXiv preprint arXiv:2311.17907*, 2023.
- [149] X. Yang, Y. Chen, C. Chen, C. Zhang, Y. Xu, X. Yang, F. Liu, and G. Lin, "Learn to optimize denoising scores for 3d generation: A unified and improved diffusion prior on nerf and 3d gaussian splatting," *arXiv preprint arXiv:2312.04820*, 2023.
- [150] Z.-X. Zou, Z. Yu, Y.-C. Guo, Y. Li, D. Liang, Y.-P. Cao, and S.-H. Zhang, "Triplane meets gaussian splatting: Fast and generalizable single-view 3d reconstruction with transformers," *arXiv preprint arXiv:2312.09147*, 2023.
- [151] H. Ling, S. W. Kim, A. Torralba, S. Fidler, and K. Kreis, "Align your gaussians: Text-to-4d with dynamic 3d gaussians and composed diffusion models," *arXiv preprint arXiv:2312.13763*, 2023.
- [152] J. Ren, L. Pan, J. Tang, C. Zhang, A. Cao, G. Zeng, and Z. Liu, "Dreamgaussian4d: Generative 4d gaussian splatting," *arXiv preprint arXiv:2312.17142*, 2023.
- [153] Y. Yin, D. Xu, Z. Wang, Y. Zhao, and Y. Wei, "4dgen: Grounded 4d content generation with spatial-temporal consistency," *arXiv preprint arXiv:2312.17225*, 2023.
- [154] H. Ouyang, K. Heal, S. Lombardi, and T. Sun, "Text2immersion: Generative immersive scene with 3d gaussians," *arXiv preprint arXiv:2312.09242*, 2023.
- [155] J. Zhang, Z. Tang, Y. Pang, X. Cheng, P. Jin, Y. Wei, W. Yu, M. Ning, and L. Yuan, "Repaint123: Fast and high-quality one image to 3d generation with progressive controllable 2d repainting," *arXiv preprint arXiv:2312.13271*, 2023.
- [156] Z. Pan, Z. Yang, X. Zhu, and L. Zhang, "Fast dynamic 3d object generation from a single-view video," *arXiv preprint arXiv:2401.08742*, 2024.
- [157] D. Xu, Y. Yuan, M. Mardani, S. Liu, J. Song, Z. Wang, and A. Vahdat, "Agg: Amortized generative 3d gaussians for single image to 3d," *arXiv preprint arXiv:2401.04099*, 2024.
- [158] J. Tang, Z. Chen, X. Chen, T. Wang, G. Zeng, and Z. Liu, "Lgm: Large multi-view gaussian model for high-resolution 3d content creation," *arXiv preprint arXiv:2402.05054*, 2024.
- [159] C. Yang, S. Li, J. Fang, R. Liang, L. Xie, X. Zhang, W. Shen, and Q. Tian, "Gaussianobject: Just taking four images to get a high-quality 3d object with gaussian splatting," *arXiv preprint arXiv:2402.10259*, 2024.
- [160] W. Zielonka, T. Bagautdinov, S. Saito, M. Zollhöfer, J. Thies, and J. Romero, "Drivable 3d gaussian avatars," *arXiv preprint arXiv:2311.08581*, 2023.
- [161] R. Jena, G. S. Iyer, S. Choudhary, B. Smith, P. Chaudhari, and J. Gee, "Splatarmor: Articulated gaussian splatting for animatable humans from monocular rgb videos," *arXiv preprint arXiv:2311.10812*, 2023.
- [162] K. Ye, T. Shao, and K. Zhou, "Animatable 3d gaussians for high-fidelity synthesis of human motions," *arXiv preprint arXiv:2311.13404*, 2023.
- [163] Z. Li, Z. Zheng, L. Wang, and Y. Liu, "Animatable gaussians: Learning pose-dependent gaussian maps for high-fidelity human avatar modeling," *arXiv preprint arXiv:2311.16096*, 2023.
- [164] J. Lei, Y. Wang, G. Pavlakos, L. Liu, and K. Daniilidis, "Gart: Gaussian articulated template models," *arXiv preprint arXiv:2311.16099*, 2023.
- [165] A. Moreau, J. Song, H. Dharmo, R. Shaw, Y. Zhou, and E. Pérez-Pellitero, "Human gaussian splatting: Real-time rendering of animatable avatars," *arXiv preprint arXiv:2311.17113*, 2023.
- [166] M. Kocabas, J.-H. R. Chang, J. Gabriel, O. Tuzel, and A. Ranjan, "Hugs: Human gaussian splats," *arXiv preprint arXiv:2311.17910*, 2023.
- [167] R. Abdal, W. Yifan, Z. Shi, Y. Xu, R. Po, Z. Kuang, Q. Chen, D.-Y. Yeung, and G. Wetzstein, "Gaussian shell maps for efficient 3d human generation," *arXiv preprint arXiv:2311.17857*, 2023.
- [168] J. Wang, X. Li, J. Xie, F. Xu, and H. Gao, "Gaussianhead: Impressive 3d gaussian-based head avatars with dynamic hybrid neural field," *arXiv preprint arXiv:2312.01632*, 2023.
- [169] S. Qian, T. Kirschstein, L. Schoneveld, D. Davoli, S. Giebenhain, and M. Nießner, "Gaussianavatars: Photorealistic head avatars with rigged 3d gaussians," *arXiv preprint arXiv:2312.02069*, 2023.
- [170] S. Zheng, B. Zhou, R. Shao, B. Liu, S. Zhang, L. Nie, and Y. Liu, "Gps-gaussian: Generalizable pixel-wise 3d gaussian splatting for real-time human novel view synthesis," *arXiv preprint arXiv:2312.02155*, 2023.
- [171] S. Hu and Z. Liu, "Gauhuman: Articulated gaussian splatting from monocular human videos," *arXiv preprint arXiv:2312.02973*, 2023.
- [172] H. Dharmo, Y. Nie, A. Moreau, J. Song, R. Shaw, Y. Zhou, and E. Pérez-Pellitero, "Headgas: Real-time animatable head avatars via 3d gaussian splatting," *arXiv preprint arXiv:2312.02902*, 2023.
- [173] Y. Jiang, Z. Shen, P. Wang, Z. Su, Y. Hong, Y. Zhang, J. Yu, and L. Xu, "Hifi4g: High-fidelity human performance rendering via compact gaussian splatting," *arXiv preprint arXiv:2312.03461*, 2023.
- [174] L. Hu, H. Zhang, Y. Zhang, B. Zhou, B. Liu, S. Zhang, and L. Nie, "Gaussianavatar: Towards realistic human avatar modeling from a single video via animatable 3d gaussians," *arXiv preprint arXiv:2312.02134*, 2023.
- [175] J. Xiang, X. Gao, Y. Guo, and J. Zhang, "Flashavatar: High-fidelity digital avatar rendering at 300fps," *arXiv preprint arXiv:2312.02214*, 2023.
- [176] S. Saito, G. Schwartz, T. Simon, J. Li, and G. Nam, "Relightable gaussian codec avatars," *arXiv preprint arXiv:2312.03704*, 2023.
- [177] Y. Chen, L. Wang, Q. Li, H. Xiao, S. Zhang, H. Yao, and Y. Liu, "Monogaussianavatar: Monocular gaussian point-based head avatar," *arXiv preprint arXiv:2312.04558*, 2023.
- [178] H. Pang, H. Zhu, A. Kortylewski, C. Theobalt, and M. Habermann, "Ash: Animatable gaussian splats for efficient and photoreal human rendering," *arXiv preprint arXiv:2312.05941*, 2023.
- [179] Z. Qian, S. Wang, M. Mihajlovic, A. Geiger, and S. Tang, "3dgs-avatar: Animatable avatars via deformable 3d gaussian splatting," *arXiv preprint arXiv:2312.09228*, 2023.
- [180] Y. Yuan, X. Li, Y. Huang, S. De Mello, K. Nagano, J. Kautz, and U. Iqbal, "Gavatar: Animatable 3d gaussian avatars with implicit mesh learning," *arXiv preprint arXiv:2312.11461*, 2023.
- [181] H. Jung, N. Brasch, J. Song, E. Perez-Pellitero, Y. Zhou, Z. Li, N. Navab, and B. Busam, "Deformable 3d gaussian splatting for animatable human avatars," *arXiv preprint arXiv:2312.15059*, 2023.
- [182] M. Li, J. Tao, Z. Yang, and Y. Yang, "Human101: Training 100+ fps human gaussians in 100s from 1 view," *arXiv preprint arXiv:2312.15258*, 2023.
- [183] Z. Zhao, Z. Bao, Q. Li, G. Qiu, and K. Liu, "Psavatar: A point-based morphable shape model for real-time head avatar creation with 3d gaussian splatting," *arXiv preprint arXiv:2401.12900*, 2024.
- [184] M. Li, S. Yao, Z. Xie, K. Chen, and Y.-G. Jiang, "Gaussianbody: Clothed human reconstruction via 3d gaussian splatting," *arXiv preprint arXiv:2401.09720*, 2024.
- [185] H. Luo, M. Ouyang, Z. Zhao, S. Jiang, L. Zhang, Q. Zhang, W. Yang, L. Xu, and J. Yu, "Gaussianhair: Hair modeling and rendering with light-aware gaussians," *arXiv preprint arXiv:2402.10483*, 2024.
- [186] Y. Chen, Z. Chen, C. Zhang, F. Wang, X. Yang, Y. Wang, Z. Cai, L. Yang, H. Liu, and G. Lin, "Gaussianeditor: Swift and controllable 3d editing with gaussian splatting," *arXiv preprint arXiv:2311.14521*, 2023.
- [187] J. Fang, J. Wang, X. Zhang, L. Xie, and Q. Tian, "Gaussianeditor: Editing 3d gaussians delicately with text instructions," *arXiv preprint arXiv:2311.16037*, 2023.

- [188] J. Huang and H. Yu, "Point'n move: Interactive scene object manipulation on gaussian splatting radiance fields," *arXiv preprint arXiv:2311.16737*, 2023.
- [189] K. Lan, H. Li, H. Shi, W. Wu, Y. Liao, L. Wang, and P. Zhou, "2d-guided 3d gaussian segmentation," *arXiv preprint arXiv:2312.16047*, 2023.
- [190] J. Zhuang, D. Kang, Y.-P. Cao, G. Li, L. Lin, and Y. Shan, "Tip-editor: An accurate 3d editor following both text-prompts and image-prompts," *arXiv preprint arXiv:2401.14828*, 2024.
- [191] B. Dou, T. Zhang, Y. Ma, Z. Wang, and Z. Yuan, "Cosseggaussians: Compact and swift scene segmenting 3d gaussians," *arXiv preprint arXiv:2401.05925*, 2024.
- [192] X. Hu, Y. Wang, L. Fan, J. Fan, J. Peng, Z. Lei, Q. Li, and Z. Zhang, "Semantic anything in 3d gaussians," *arXiv preprint arXiv:2401.17857*, 2024.
- [193] J. Straub, T. Whelan, L. Ma, Y. Chen, E. Wijnmans, S. Green, J. J. Engel, R. Mur-Artal, C. Ren, S. Verma *et al.*, "The replica dataset: A digital replica of indoor spaces," *arXiv preprint arXiv:1906.05797*, 2019.
- [194] J. Park, Q.-Y. Zhou, and V. Koltun, "Colored point cloud registration revisited," in *ICCV*, 2017, pp. 143–152.
- [195] E. Sucar, S. Liu, J. Ortiz, and A. J. Davison, "imap: Implicit mapping and positioning in real-time," in *ICCV*, 2021, pp. 6229–6238.
- [196] X. Yang, H. Li, H. Zhai, Y. Ming, Y. Liu, and G. Zhang, "Vox-fusion: Dense tracking and mapping with voxel-based neural implicit representation," in *2022 IEEE International Symposium on Mixed and Augmented Reality (ISMAR)*, 2022, pp. 499–507.
- [197] Z. Zhu, S. Peng, V. Larsson, W. Xu, H. Bao, Z. Cui, M. R. Oswald, and M. Pollefeys, "Nice-slam: Neural implicit scalable encoding for slam," in *CVPR*, 2022, pp. 12786–12796.
- [198] M. M. Johari, C. Carta, and F. Fleuret, "Eslam: Efficient dense slam system based on hybrid representation of signed distance fields," in *CVPR*, 2023, pp. 17408–17419.
- [199] E. Sandström, Y. Li, L. Van Gool, and M. R. Oswald, "Point-slam: Dense neural point cloud-based slam," in *ICCV*, 2023, pp. 18433–18444.
- [200] H. Wang, J. Wang, and L. Agapito, "Co-slam: Joint coordinate and sparse parametric encodings for neural real-time slam," in *CVPR*, 2023, pp. 13293–13302.
- [201] X. Huang, X. Cheng, Q. Geng, B. Cao, D. Zhou, P. Wang, Y. Lin, and R. Yang, "The apollo-scape dataset for autonomous driving," in *Proceedings of the IEEE conference on computer vision and pattern recognition workshops*, 2018, pp. 954–960.
- [202] J. Wang, J. Liu, and N. Kato, "Networking and communications in autonomous driving: A survey," *IEEE Communications Surveys & Tutorials*, vol. 21, no. 2, pp. 1243–1274, 2018.
- [203] P. Sun, H. Kretzschmar, X. Dotiwalla, A. Chouard, V. Patnaik, P. Tsui, J. Guo, Y. Zhou, Y. Chai, B. Caine *et al.*, "Scalability in perception for autonomous driving: Waymo open dataset," in *CVPR*, 2020, pp. 2446–2454.
- [204] H. Caesar, V. Bankiti, A. H. Lang, S. Vora, V. E. Liong, Q. Xu, A. Krishnan, Y. Pan, G. Baldan, and O. Beijbom, "nusenes: A multimodal dataset for autonomous driving," in *CVPR*, 2020, pp. 11621–11631.
- [205] J. Guo, U. Kurup, and M. Shah, "Is it safe to drive? an overview of factors, metrics, and datasets for driveability assessment in autonomous driving," *IEEE Transactions on Intelligent Transportation Systems*, vol. 21, no. 8, pp. 3135–3151, 2019.
- [206] K. Muhammad, A. Ullah, J. Lloret, J. Del Ser, and V. H. C. de Albuquerque, "Deep learning for safe autonomous driving: Current challenges and future directions," *IEEE Transactions on Intelligent Transportation Systems*, vol. 22, no. 7, pp. 4316–4336, 2020.
- [207] S. Teng, X. Hu, P. Deng, B. Li, Y. Li, Y. Ai, D. Yang, L. Li, Z. Xuanyuan, F. Zhu *et al.*, "Motion planning for autonomous driving: The state of the art and future perspectives," *IEEE Transactions on Intelligent Vehicles*, 2023.
- [208] Y. Hu, J. Yang, L. Chen, K. Li, C. Sima, X. Zhu, S. Chai, S. Du, T. Lin, W. Wang *et al.*, "Planning-oriented autonomous driving," in *CVPR*, 2023, pp. 17853–17862.
- [209] X. Ma, W. Ouyang, A. Simonelli, and E. Ricci, "3d object detection from images for autonomous driving: a survey," *IEEE Transactions on Pattern Analysis and Machine Intelligence*, 2023.
- [210] J. Mao, S. Shi, X. Wang, and H. Li, "3d object detection for autonomous driving: A comprehensive survey," *International Journal of Computer Vision*, pp. 1–55, 2023.
- [211] D. Fu, X. Li, L. Wen, M. Dou, P. Cai, B. Shi, and Y. Qiao, "Drive like a human: Rethinking autonomous driving with large language models," in *Proceedings of the IEEE/CVF Winter Conference on Applications of Computer Vision*, 2024, pp. 910–919.
- [212] J. Wang, Y. Yuan, Z. Luo, K. Xie, D. Lin, U. Iqbal, S. Fidler, and S. Khamis, "Learning human dynamics in autonomous driving scenarios," in *ICCV*, 2023, pp. 20796–20806.
- [213] X. Zhou, Z. Lin, X. Shan, Y. Wang, D. Sun, and M.-H. Yang, "Drivinggaussian: Composite gaussian splatting for surrounding dynamic autonomous driving scenes," *arXiv preprint arXiv:2312.07920*, 2023.
- [214] Y. Yan, H. Lin, C. Zhou, W. Wang, H. Sun, K. Zhan, X. Lang, X. Zhou, and S. Peng, "Street gaussians for modeling dynamic urban scenes," *arXiv preprint arXiv:2401.01339*, 2024.
- [215] H. Zhou, J. Shao, L. Xu, D. Bai, W. Qiu, B. Liu, Y. Wang, A. Geiger, and Y. Liao, "Hugs: Holistic urban 3d scene understanding via gaussian splatting," *arXiv preprint arXiv:2403.12722*, 2024.
- [216] Y. Wang, Y. Long, S. H. Fan, and Q. Dou, "Neural rendering for stereo 3d reconstruction of deformable tissues in robotic surgery," in *MICCAI*, 2022, pp. 431–441.
- [217] C. Yang, K. Wang, Y. Wang, X. Yang, and W. Shen, "Neural lerplane representations for fast 4d reconstruction of deformable tissues," in *MICCAI*, 2023, pp. 46–56.
- [218] R. Zha, X. Cheng, H. Li, M. Harandi, and Z. Ge, "Endosurf: Neural surface reconstruction of deformable tissues with stereo endoscope videos," in *MICCAI*, 2023, pp. 13–23.
- [219] Y. Huang, B. Cui, L. Bai, Z. Guo, M. Xu, and H. Ren, "Endo-4dgs: Distilling depth ranking for endoscopic monocular scene reconstruction with 4d gaussian splatting," *arXiv preprint arXiv:2401.16416*, 2024.
- [220] Y. Liu, C. Li, C. Yang, and Y. Yuan, "Endogaussian: Gaussian splatting for deformable surgical scene reconstruction," *arXiv preprint arXiv:2401.12561*, 2024.
- [221] L. Zhu, Z. Wang, Z. Jin, G. Lin, and L. Yu, "Deformable endoscopic tissues reconstruction with gaussian splatting," *arXiv preprint arXiv:2401.11535*, 2024.
- [222] K. Wang, C. Yang, Y. Wang, S. Li, Y. Wang, Q. Dou, X. Yang, and W. Shen, "Endogslam: Real-time dense reconstruction and tracking in endoscopic surgeries using gaussian splatting," *arXiv preprint arXiv:2403.15124*, 2024.
- [223] G. N. Hounsfield, "Computed medical imaging," *Science*, vol. 210, no. 4465, pp. 22–28, 1980.
- [224] Z. Zhang, X. Liang, X. Dong, Y. Xie, and G. Cao, "A sparse-view ct reconstruction method based on combination of densenet and deconvolution," *IEEE transactions on medical imaging*, vol. 37, no. 6, pp. 1407–1417, 2018.
- [225] A. Molaei, A. Aminimehr, A. Tavakoli, A. Kazerouni, B. Azad, R. Azad, and D. Merhof, "Implicit neural representation in medical imaging: A comparative survey," in *ICCV*, 2023, pp. 2381–2391.
- [226] Y. Cai, Y. Liang, J. Wang, A. Wang, Y. Zhang, X. Yang, Z. Zhou, and A. Yuille, "Radiative gaussian splatting for efficient x-ray novel view synthesis," *arXiv preprint arXiv:2403.04116*, 2024.
- [227] Y. Li, X. Fu, S. Zhao, R. Jin, and S. K. Zhou, "Sparse-view ct reconstruction with 3d gaussian volumetric representation," *arXiv preprint arXiv:2312.15676*, 2023.
- [228] J. Sturm, N. Engelhard, F. Endres, W. Burgard, and D. Cremers, "A benchmark for the evaluation of rgb-d slam systems," in *2012 IEEE/RSJ international conference on intelligent robots and systems*, 2012, pp. 573–580.
- [229] J. Fang, T. Yi, X. Wang, L. Xie, X. Zhang, W. Liu, M. Niefßner, and Q. Tian, "Fast dynamic radiance fields with time-aware neural voxels," in *SIGGRAPH Asia 2022 Conference Papers*, 2022, pp. 1–9.
- [230] A. Cao and J. Johnson, "Hexplane: A fast representation for dynamic scenes," in *CVPR*, 2023, pp. 130–141.
- [231] F. Wang, Z. Chen, G. Wang, Y. Song, and H. Liu, "Masked space-time hash encoding for efficient dynamic scene reconstruction," in *NeurIPS*, 2023.
- [232] Z. Wang, A. C. Bovik, H. R. Sheikh, and E. P. Simoncelli, "Image quality assessment: from error visibility to structural similarity," *IEEE TIP*, vol. 13, no. 4, pp. 600–612, 2004.
- [233] R. Zhang, P. Isola, A. A. Efros, E. Shechtman, and O. Wang, "The unreasonable effectiveness of deep features as a perceptual metric," in *CVPR*, 2018, pp. 586–595.
- [234] J. T. Barron, B. Mildenhall, M. Tancik, P. Hedman, R. Martin-Brualla, and P. P. Srinivasan, "Mip-nerf: A multiscale representa-

- tion for anti-aliasing neural radiance fields,” in *ICCV*, 2021, pp. 5855–5864.
- [235] K. Rematas, A. Liu, P. P. Srinivasan, J. T. Barron, A. Tagliasacchi, T. Funkhouser, and V. Ferrari, “Urban radiance fields,” in *CVPR*, 2022, pp. 12 932–12 942.
- [236] Z. Xie, J. Zhang, W. Li, F. Zhang, and L. Zhang, “S-nerf: Neural radiance fields for street views,” in *ICLR*, 2023.
- [237] H. Turki, J. Y. Zhang, F. Ferroni, and D. Ramanan, “Suds: Scalable urban dynamic scenes,” in *CVPR*, 2023, pp. 12 375–12 385.
- [238] S. Peng, Y. Zhang, Y. Xu, Q. Wang, Q. Shuai, H. Bao, and X. Zhou, “Neural body: Implicit neural representations with structured latent codes for novel view synthesis of dynamic humans,” in *CVPR*, 2021, pp. 9054–9063.
- [239] S. Peng, J. Dong, Q. Wang, S. Zhang, Q. Shuai, X. Zhou, and H. Bao, “Animatable neural radiance fields for modeling dynamic human bodies,” in *ICCV*, 2021, pp. 14 314–14 323.
- [240] A. Yu, V. Ye, M. Tancik, and A. Kanazawa, “pixelnerf: Neural radiance fields from one or few images,” in *CVPR*, 2021, pp. 4578–4587.
- [241] Y. Kwon, D. Kim, D. Ceylan, and H. Fuchs, “Neural human performer: Learning generalizable radiance fields for human performance rendering,” in *NeurIPS*, 2021, pp. 24 741–24 752.
- [242] C.-Y. Weng, B. Curless, P. P. Srinivasan, J. T. Barron, and I. Kemelmacher-Shlizerman, “Humannerf: Free-viewpoint rendering of moving people from monocular video,” in *CVPR*, 2022, pp. 16 210–16 220.
- [243] C. Geng, S. Peng, Z. Xu, H. Bao, and X. Zhou, “Learning neural volumetric representations of dynamic humans in minutes,” in *CVPR*, 2023, pp. 8759–8770.
- [244] A. Guédon and V. Lepetit, “Sugar: Surface-aligned gaussian splatting for efficient 3d mesh reconstruction and high-quality mesh rendering,” *arXiv preprint arXiv:2311.12775*, 2023.
- [245] T. Xie, Z. Zong, Y. Qiu, X. Li, Y. Feng, Y. Yang, and C. Jiang, “Physgaussian: Physics-integrated 3d gaussians for generative dynamics,” *arXiv preprint arXiv:2311.12198*, 2023.
- [246] J. Abou-Chakra, K. Rana, F. Dayoub, and N. Sünderhauf, “Physically embodied gaussian splatting: Embedding physical priors into a visual 3d world model for robotics,” in *Conference on Robot Learning*, no. 7th, 2023.
- [247] G. Lu, S. Zhang, Z. Wang, C. Liu, J. Lu, and Y. Tang, “Manigaussian: Dynamic gaussian splatting for multi-task robotic manipulation,” *arXiv preprint arXiv:2403.08321*, 2024.
- [248] Y. Liu, H. Guan, C. Luo, L. Fan, J. Peng, and Z. Zhang, “City-gaussian: Real-time high-quality large-scale scene rendering with gaussians,” *arXiv preprint arXiv:2404.01133*, 2024.
- [249] Y. Sun, X. Wang, Y. Zhang, J. Zhang, C. Jiang, Y. Guo, and F. Wang, “icomma: Inverting 3d gaussians splatting for camera pose estimation via comparing and matching,” *arXiv preprint arXiv:2312.09031*, 2023.
- [250] C. Pokhariya, I. N. Shah, A. Xing, Z. Li, K. Chen, A. Sharma, and S. Sridhar, “Manus: Markerless hand-object grasp capture using articulated 3d gaussians,” *arXiv preprint arXiv:2312.02137*, 2023.
- [251] W. Jiang, B. Lei, and K. Daniilidis, “Fisherrf: Active view selection and uncertainty quantification for radiance fields using fisher information,” *arXiv preprint arXiv:2311.17874*, 2023.
- [252] Y. Feng, X. Feng, Y. Shang, Y. Jiang, C. Yu, Z. Zong, T. Shao, H. Wu, K. Zhou, C. Jiang *et al.*, “Gaussian splashing: Dynamic fluid synthesis with gaussian splatting,” *arXiv preprint arXiv:2401.15318*, 2024.